Low-energy electron collisions with sodium: Scattering of spin-polarized electrons

Hsiao-Ling Zhou,* Barbara L. Whitten,† Wayne K. Trail,‡ Michael A. Morrison,§ Keith B. MacAdam,‖ Klaus Bartschat,¶ and David W. Norcross**

Joint Institute for Laboratory Astrophysics, University of Colorado and National Institute of Standards and Technology, Boulder, Colorado 80309-0440

(Received 27 December 1994)

The electron-sodium system is a prototype of nonrelativistic electron scattering from a quasi-one-electron atomic target and is tractable both experimentally and theoretically. Recently, this system has been studied in a series of sophisticated measurements that together approach complete experiments for elastic ($3s \rightarrow 3s$) and inelastic ($3s \rightarrow 3p$) scattering. We apply here the theory of orientation and alignment (OA) in atomic collisions to this system using scattering matrices from coupled channel R-matrix calculations described in the first paper in this series [W. K. Trail *et al.*, Phys. Rev. A **49**, 3620 (1994)]. To facilitate the extension of OA theory to other transitions and systems and to clarify its relationship to canonical scattering theory, we present a reformulation in terms of the state spaces identified by a particular scattering event. Following the application of this formulation to paradigmatic OA experiments, we compare our results to those from existing measurements and other theoretical calculations. To contextualize these experiments and aid in identifying promising regions for future measurements, we also present a comprehensive three-dimensional overview of the calculated differential OA parameters for energies from threshold to 8.6 eV.

PACS number(s): 34.80.Bm, 34.80.Dp, 34.80.Nz

I. INTRODUCTION

This is the second of a trilogy of papers, the cumulative goal of which is to provide a comprehensive look at the dynamics of low-energy electron scattering from a prototypical light alkali-metal target, the sodium atom. In the first paper [1] we described the theory we use to solve the continuum Schrödinger equation—the close-coupling R-matrix method—and discussed the approximations inherent in its treatment of the continuum. We further presented integrated and differential elastic and inelastic cross sections for scattering from the $3\,^2S$ ground state at energies from threshold to 8.6 eV. In addition to making detailed comparisons to available results from experiments and other theoretical studies, we examined results throughout this entire energy range, within which several inelastic channels become open, in order to identify trends and structures that distinguish and characterize this system.

The cross sections considered in Ref. [1] do not fully describe the physics of e-Na collisions. Until the past two decades, most scattering experiments measured "conventional" differential (DCSs) and/or integrated cross sections (ICSs) that implicitly involve averages over initial and sums over final spin and orbital magnetic substates. These necessary averages obscure much of the dynamical information contained in the scattering amplitudes. More recently, however, experiments [2–17] have become feasible that use a variety of techniques to prepare the target atoms in an initial nonequilibrium distribution of magnetic and/or spin substates or to detect the magnetic and/or spin substates of the results of a scattering event. Such experiments have dramatically increased our understanding of atomic collisions and provide data that test theories at a more fundamental level than was heretofore possible [18–32].

In the present paper, therefore, we extend this inquiry to a class of experiments that uses initial-state preparation and/or final-state analysis to look more deeply into the physics of low-energy e-Na scattering. Rather than DCS's, these experiments measure less familiar quantities such as exchange asymmetries and triplet-singlet phase angles; the importance of these "orientation and alignment (OA) parameters" rests in their often subtle physical interpretation and in their relationship to the scattering amplitudes for the transitions in question—matters we shall address in Sec. II. As in Ref. [1], we focus here on scattering from the ground state, considering the two transitions for which data are available: elastic scattering and the dipole transition $3\,^2S \rightarrow 3\,^2P$. In the final paper of this series we shall extend this formalism and attendant calculations to other transitions, including scattering

*Present address: Department of Physics & Astrophysics, Georgia State University, Atlanta, GA 30303.

†Permanent address: Physics Department, Colorado College, Colorado Springs, CO 80903.

‡Present address: Department of Physics & Astronomy, University of Oklahoma, Norman, OK 73019-0225.

§Permanent address: Department of Physics & Astronomy, University of Oklahoma, Norman, OK 73019-0225.

‖Permanent address: Department of Physics & Astronomy, University of Kentucky, Lexington, KY 40506-0055.

¶Permanent address: Department of Physics & Astronomy, Drake University, Des Moines, IA 50311.

**Present address: Quantum Physics Division, National Institute of Standards and Technology, Gaithersburg, MD 20899.

from excited initial states.

Historically, the study of orientation and alignment parameters received a major impetus in 1969 and 1970 from a series of papers in which Bederson [33–35] explicated strategies for measuring sufficient independent quantities to fully describe the complex scattering amplitudes for elastic and inelastic electron–alkali-metal scattering. As the amplitudes themselves resist direct access, great care and ingenuity is required to identify observables that are amenable to practical experiment and physical interpretation. Recent progress on both experimental and theoretical fronts towards realizing such "complete" scattering experiments has been swift and, for elastic scattering at least, decisive—as adumbrated in several recent reviews and commentaries.

The present study builds on this earlier work in two ways. First, we present in Sec. II a variant of the now-standard density-matrix theory of orientation and alignment in electron-atom collisions. This formulation, summarized in Sec. II A, is based on operators in the state spaces of a particular scattering event. We have found that it admits very straightforward, algebraically simple analysis of experiments to measure OA parameters (see Sec. III), highlights the relationship of these parameters to the more-familiar amplitudes that appear in the scattering boundary conditions, and, most importantly, is easily generalizable to other transitions (e.g., involving excited initial states) and systems. Second, we present a comprehensive set of high-precision OA parameters for the elastic and lowest-lying dipole transitions and in Sec. V compare those recently calculated values to results from experiments and the other extant theoretical study where available. In particular, we compare to results from coupled-channel optical calculations by Bray and McCarthy [38,39], which were performed using a completely different formalism based on solving the momentum space Lippmann-Schwinger equation for the T matrix that, unlike the present method, includes continuum target states. The most rigorous such theory for the calculation of scattering amplitudes, the convergent close-coupling method of Bray [40,41], allows for systematic inclusion of the continuum by means of approximate square-integrable states, as detailed by Bray and Stebovics [42]. Unfortunately, data from such calculations are available for comparison only at a few energies. So we precede these comparisons by a comprehensive overview of trends and features in the elastic and the inelastic OA parameters for scattering from the ground state, exploiting the ability of the R-matrix method to efficiently generate scattering quantities at a large number of energies to survey in detail the entire energy range from threshold to 8.6 eV. As we showed in Ref. [1], DCSs and ICSs in this energy range are marked by a rich variety of structures; in Sec. IV of the present paper we show the effect of these structures on OA parameters and, through them, on features of the dynamics not evident in conventional cross sections. This overview both provides a context for the comparisons to experiment in Sec. V (most of which are limited to a single energy at which the results are somewhat anomalous) and suggest trends in the OA parameters that we hope will stimulate future measurements.

The most widely used previous calculation of e-Na scattering amplitudes was published in 1972 by Moores and Norcross [43]. As detailed in Ref. [1], the present calculations reach beyond that earlier work in two ways. The most significant of these is our improved representation of the target and of the angular-momentum properties of the projectile. Increases in computational power since the work of Moores and Norcross have made possible convergence to high precision of all cross sections and OA parameters in both of the expansions that define the close-coupling theory of electron-atom scattering, i.e., in the set of bound states of the target and in the set of angular-momentum eigenstates (partial waves) of the scattering electron. Since we dealt with convergence issues pertaining to DCSs and ICSs in Ref. [1], we address here only convergence matters relating to the calculation of OA parameters, which often exhibit greater sensitivity to convergence than conventional cross sections. The second difference between the present formulation and that of Moores and Norcross—the representation of bound-free exchange and polarization effects in the e-Na interaction potential—has been discussed in Sec. III of Ref. [1]. Unless otherwise stated, we use atomic units for length (a_0) and cross sections (a_0^2), where the first Bohr radius is $a_0 = 5.291\,77 \times 10^{-11}$ m.

II. THEORY: COLLISIONS INVOLVING SPIN-POLARIZED ELECTRONS AND STATE-SELECTED ATOMS

During the past 15 years, an extensive literature on scattering of spin-polarized electrons by atoms has developed. Several authors have reviewed recent advances in this field, including Kessler [24,25], Slevin [20], Blum and Kleinpoppen [19], Hanne [21,23], and contributors to Ref. [18]. In a recent review [27] Andersen, Gallagher, and Hertel have attempted to standardize notation for describing alignment and orientation in direct excitation by electron impact; Bartschat has made further contributions to this effort [32].

Our primary goals in this section are, first, to establish language and notation we shall use in discussing results for electron scattering from ground-state Na in Secs. IV and V and from excited-state Na in the sequel to the present paper. Crucial to interpreting the range of scattering quantities we shall present, which include but are not limited to energies at which experiments have been performed, is the interplay between the system wave function, the density matrices that represent the initial and final states, and the orientation and alignment parameters that afford physical insight into the dynamics. Hence this relationship will receive special attention in this section.

Sodium is an almost ideal quasi-one-electron atom. Its neonlike $1s^2 2s^2 2p^6$ core is very tightly bound, so its valence electron is very nearly hydrogenic. Further, its nuclear charge ($Z = 11$) is small enough that the separation between adjacent Na atomic terms is much larger than the separation between fine and hyperfine levels; hence for scattering events of interest here, spin-orbit in-

teractions are negligible. Moreover, these e-Na collisions occur much more rapidly (typical collision times are $\simeq 10^{-15}$ sec) than the natural lifetimes of the states involved or the fine or hyperfine precession times (typical spin precession times are $\simeq 10^{-9}$–10^{-12} sec), so we can invoke an argument derived from the Percival-Seaton hypothesis [28] to the effect that coupling of the spins of the scattering and valence electrons to form a total spin takes precedence over coupling of the individual spins to the corresponding orbital angular momenta [29–31]. We can further neglect continuum spin-orbit interactions, so the aforementioned total spin is a constant of the collision. Finally, for low-energy collisions we can neglect nuclear spin and excitations of the Ne-like core of the sodium atom and consider the target as an idealized one-electron system with total spin of $\frac{1}{2}$. In this sense the e-Na interaction is a prototypical nonrelativistic two-electron interaction.

Within these approximations we can describe the bound states of the atom using the LS representation, where we denote these states using quantum numbers associated with the (total) target orbital and spin angular momenta $\mathbf{L}$ and $\mathbf{S}$ and their projections M_L and M_S on an (arbitrary) axis of quantization. Since the core does not participate in the excitations we shall consider, the target electronic configuration Γ is specified by the principal quantum number n of the valence electron. As in Ref. [1], here we shall denote collectively the quantum numbers required to specify such a state by $\alpha=(\Gamma,L,S,M_L,M_S)$ and use capital script letters for quantum numbers of the electron-atom system.

In many of the experiments to be discussed in Sec. III, the initial and final spin projections of the projectile and/or the target atoms are detected. In this case we can identify three types of experiments [33–35]

$$e(\uparrow)+A(\uparrow)\rightarrow e(\uparrow)+A(\uparrow)\,, \tag{1a}$$

$$e(\uparrow)+A(\downarrow)\rightarrow e(\uparrow)+A(\downarrow)\,, \tag{1b}$$

$$e(\uparrow)+A(\downarrow)\rightarrow e(\downarrow)+A(\uparrow)\,. \tag{1c}$$

Other possibilities, such as

$$e(\uparrow)+A(\uparrow)\rightarrow e(\downarrow)+A(\downarrow)\,, \tag{1d}$$

are forbidden because in the absence of spin-orbit coupling, the total spin of the system and its projection are conserved. Note that the first experiment Eq. (1a) isolates scattering in the triplet spin channel. Similarly, the second experiment Eq. (1b) isolates direct scattering and the third Eq. (1c) exchange scattering. Thus, by specifying the spin projections of the projectile and target one can study scattering in these channels dominated by distinct physical effects arising from the quantum-mechanical antisymmetrization requirement.

A. Scattering amplitudes and the description of scattering events

To analyze any of these experiments theoretically we require the scattering amplitude that connects asymptotic free states before and after the collision. These states depend on the wave vector of the scattering electron $\mathbf{k}$, its spin projection m_s, and the target quantum numbers α. The scattering amplitude is defined by the asymptotic behavior of the e-Na wave function, which depends on the space and spin coordinates of the bound electrons τ_e and of the projectile $(\mathbf{r},\sigma)$. Using $\phi_\alpha(\tau_e)$ for the target wave functions and zero subscripts to denote the initial channel, we can write these boundary conditions as

$$\Psi_{\mathbf{k}_0,m_{s_0},\alpha_0}(\tau_e,\mathbf{r},\sigma)\underset{r\rightarrow\infty}{\rightarrow}\phi_{\alpha_0}(\tau_e)\chi_{m_{s_0}}(\sigma)e^{i\mathbf{k}_0\cdot\mathbf{r}} + \sum_\alpha f(\mathbf{k}m_s,\alpha\leftarrow\mathbf{k}_0m_{s_0},\alpha_0) \times\phi_\alpha(\tau_e)\chi_{m_s}(\sigma)\frac{e^{ikr}}{r}\,. \tag{2}$$

The scattering amplitudes $f(\mathbf{k}m_s,\alpha\leftarrow\mathbf{k}_0m_{s_0},\alpha_0)$, which contain all physically accessible information about all energetically allowed scattering events, depend in general on the electron scattering angles θ and ϕ. For collisions considered in this paper this amplitude depends only on the angle between the initial and the final projectile momenta $\mathbf{k}_0$ and $\mathbf{k}$, i.e., the polar angle θ of a coordinate system whose z axis is aligned with $\mathbf{k}_0$.

Since in our formulation the total spin of the e-Na system is a constant of the motion, it makes sense to switch to a description in which the spins of the scattering and valence electrons have been coupled (via the Clebsch-Gordan series) to form a total spin with quantum numbers $\mathcal{S}$ and $\mathcal{M}_\mathcal{S}$. The asymptotic free states are then simply direct products of spatial and coupled-spin states

$$|\mathbf{k},nLM_L;\mathcal{S},\mathcal{M}_\mathcal{S}\rangle = |\mathbf{k},n,L,M_L\rangle \otimes\sum_{m_s,M_S}C(\tfrac{1}{2}S\mathcal{S};m_sM_S\mathcal{M}_\mathcal{S})|m_s\rangle\otimes|SM_S\rangle\,, \tag{3}$$

where for Na, of course, the atomic spin is $S=\frac{1}{2}$ and the coupled-spin asymptotic free states are zero unless

$$m_s+M_S=\mathcal{M}_\mathcal{S}\,. \tag{4}$$

In the coupled-spin description we label scattering channels by the spin multiplicity $2\mathcal{S}+1$ for $\mathcal{S}=0$ (singlet) and 1 (triplet), and scattering occurs independently in channels of different multiplicity. [Note, however, that the spin projection of the *scattering* electron can change by exchange as in process (1c).] The absence of a preferred direction in space means that the scattering amplitudes do not depend on $\mathcal{M}_\mathcal{S}$, so we can write

$$f(\mathbf{k},nLSM_L;\mathcal{S}\mathcal{M}_\mathcal{S}\leftarrow\mathbf{k}_0,n_0L_0S_0M_{L_0};\mathcal{S}\mathcal{M}_\mathcal{S}) = {}^{2\mathcal{S}+1}f_{nLSM_L\leftarrow n_0L_0S_0M_{L_0}}(\theta)\,. \tag{5}$$

[When the particular transition $n_0L_0\rightarrow nL$ is clear from the context, we shall retain as subscripts only the magnetic quantum numbers M_{L_0} and M_L, writing (5) as ${}^{2\mathcal{S}+1}f_{M_L,M_{L_0}}(\theta)$.]

To determine these amplitudes for the transition of in-

terest we solve the continuum e-Na Schrödinger equation using a formalism we have detailed in Ref. [1]. In these calculations, we take maximum advantage of the constants of the motion of the system by working in a representation different from that of Eq. (3), one in which the orbital angular momenta of the projectile and scattering electron are further coupled to form the total system orbital angular momentum, with quantum number $\mathcal{L}$. In the resulting formalism, the constants of the collision $\mathcal{L}$, $\mathcal{S}$, and the parity Π identify independent scattering functions and transition matrices. Section III of Ref. [1] relates these matrices, the fundamental output of the calculations, to the scattering amplitudes that are the subject of the present discussion.

The number of independent amplitudes required to fully characterize a collision depends on the orbital magnetic quantum numbers of the Na valence electron in the initial and the final states. Thus an $n_0s \rightarrow ns$ transition such as the elastic $3s \rightarrow 3s$ process to be considered in Sec. V allows only $M_{L_0}=M_L=0$ and is fully described by two complex scattering amplitudes ${}^1f_{0,0}(\theta)$ and ${}^3f_{0,0}(\theta)$. Although the real and the imaginary parts of these amplitudes define four independent quantities, only three are measurable, because these amplitudes share a global phase factor. (By contrast, to describe an $n_0s \rightarrow np$ transition, with $M_{L_0}=0$ and $M_L=-1,0,+1$ requires six complex amplitudes.) In general, for a transition $n_0L_0 \rightarrow nL$ we require two independent sets of amplitudes—in the coupled-spin representation (5), singlet and triplet amplitudes. Each set contains $(2L_0+1)(2L+1)$ individual amplitudes (5) identified by M_{L_0} and M_L. Measurement of all the singlet and the triplet amplitudes would constitute a complete $n_0L_0 \rightarrow nL$ scattering experiment.

The number of independent amplitudes is reduced because reflection symmetry in the scattering plane (defined by $\mathbf{k}_0$ and $\mathbf{k}$) is preserved, since this reflection operator commutes with the system Hamiltonian. This symmetry, for example, shrinks the six independent $n_0s \rightarrow np$ amplitudes to four. To demonstrate this we must choose a coordinate system. Most scattering calculations are carried out in the *collision frame* shown in Fig. 1(a), which is defined by $\hat{z}^c=\hat{\mathbf{k}}_0$ and $\hat{y}^c=\hat{\mathbf{k}}_0\times\hat{\mathbf{k}}$. In this frame $(\hat{z}^c,\hat{x}^c)$ defines the scattering plane; reflection symmetry in the scattering plane requires that $n_0s \rightarrow np$ scattering amplitudes for $M_L \neq 0$, calculated in the collision frame, be related by

$$ {}^{2\mathcal{S}+1}f_{-1,0}=-{}^{2\mathcal{S}+1}f_{+1,0} \quad \text{(collision frame)} . \tag{6}$$

The theoretical analysis of experiments can also be formulated in the *natural frame* shown in Fig. 1(b) [2–3,32], which results in structurally simpler singlet and triplet transition matrices than does the collision-frame formulation [6]. The axes of the natural frame, which are trivially related to those of the collision frame by the Wigner rotation matrices [44,45], are $\hat{x}^n=\hat{\mathbf{k}}_0$ and $\hat{z}^n=\hat{\mathbf{k}}_0\times\hat{\mathbf{k}}$, with $\hat{y}^n$ to complete a right-handed coordinate system. Reflection in the scattering plane leaves unchanged a state with $M_L=\pm 1$ but changes the sign of one with $M_L=0$. So for an $s \rightarrow p$ transition, reflection symmetry implies that

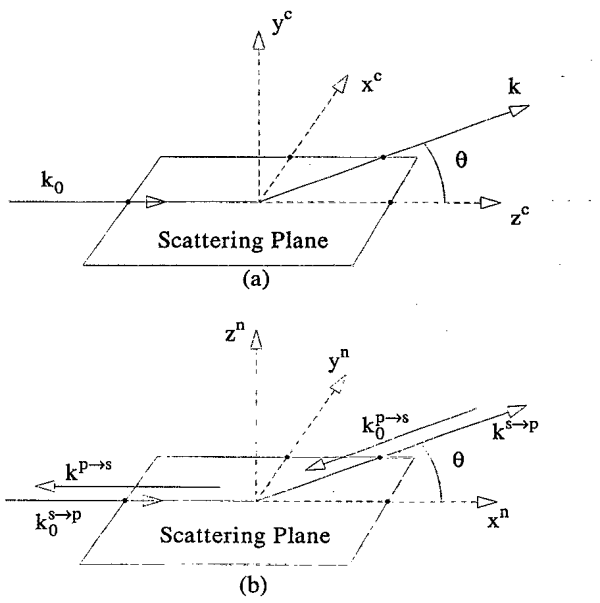

FIG. 1. (a) Schematic e-Na collision in the "collision" frame. An electron with wave vector $\mathbf{k}_0$ is incident along the $\hat{z}^c$ axis. The outgoing direction and energy are given by $\mathbf{k}$. The wave vectors $\mathbf{k}_0$ and $\mathbf{k}$ define the scattering plane (the xz plane) in this frame. (b) Schematic of inelastic and superelastic scattering in the "natural" frame. In this frame, the electron is incident along the $\hat{x}^n$ direction and undergoes an inelastic collision. The outgoing direction determines the xy plane.

$$ {}^{2\mathcal{S}+1}f_{0,0}(\theta)=0 \quad \text{(natural frame)} . \tag{7}$$

Note that in the natural frame, the scattering angle does not coincide with the polar angle of spherical coordinates. We shall continue to use θ to denote the scattering angle.

B. Description of experiments using density operators

Here and in the final paper in this series, we shall be describing theoretically a class of state-selected crossed-beam experiments in which the intensity and/or polarization of the scattered electrons is measured as a function of incident energy and scattering angle. We wish to allow for several combinations of state preparation and analysis: e.g., the use of a spin-polarized electron beam, the initial preparation of the target state in a nonequilibrium distribution of magnetic sublevels (e.g., by exciting the atom beam with polarized laser light), and the spin analysis of the final state of the system (by measuring the polarization of the scattered electrons or the polarization of the fluorescence photon emitted by the atom, perhaps in coincidence with the scattered electron). As several theorists have elucidated, such descriptions either require or are more easily formulated using density matrices [46,47]; for example, Hertel, Kelley, and McClelland [6] have detailed the implementation of such a description for superelastic $3p \rightarrow 3s$ transitions in e-Na collisions. We present here a variant of this theory based on operators in the electron-atom state spaces identified by the entrance

and exit channels of the scattering event

$$\mathbf{k}_0, n_0 L_0 \rightarrow \mathbf{k}, nL \ . \tag{8}$$

This formulation facilitates application to a variety of experiments, relating the OA parameters to familiar scattering amplitudes in Eqs. (2) and (5) and/or to measured intensities (through operational definitions), and, most importantly, generalization to arbitrary transitions (e.g., from excited initial states) and to other atomic systems where one or more of the approximations appropriate to the e-Na problem may fail. To illustrate the practical application of this formalism, we implement it for each of the classes of experiments whose results we examine in Sec. V.

1. State spaces and density and transition operators

The asymptotic states of the transition Eq. (8) are represented by either kets (if they are pure states) or density operators (if mixed states) in two finite-dimensional state spaces: $\mathcal{E}^{(eA)}_{n_0 L_0}$ for the entrance channel and $\mathcal{E}^{(eA)}_{nL}$ for the exit channel. Since the electron and the atom are uncorrelated asymptotically, it is useful to decompose the state spaces for a particular entrance and exit channel as

$$\mathcal{E}^{(eA)}_{nL} = \mathcal{E}^{(e)} \otimes \mathcal{E}^{(A)}_{nL} \ . \tag{9}$$

Since the initial and the final wave vectors are specified by the scattering event (8), these state spaces are finite dimensional. Each is spanned by bases in either the uncoupled-spin (US) or the coupled-spin (CS) representations. Thus, for $\mathcal{E}^{(eA)}_{nL}$, whose dimensionality is $4(2L+1)$, we can use either the US basis $\{|m_s, nLM_L M_S\rangle\}$ or the CS basis $\{|nLM_L; \mathcal{S}\mathcal{M}_{\mathcal{S}}\rangle\}$ as convenient.

The density operator of the system for either the initial or the final state is constructed from density operators for the electron and atom, either of which may reflect state preparation or analysis. For the scattering electron with wave vector $\mathbf{k}$ in an arbitrary spin state, the density operator is

$$\hat{\rho}^{(e)} = \sum_{m_s, m_s'} \rho^{(e)}_{m_s, m_s'} |\mathbf{k}, m_s\rangle\langle \mathbf{k}, m_s'| \ . \tag{10}$$

For the atom in state nL the (unnormalized) density operator is [48]

$$\hat{\rho}^{(A)}_{nL} = \sum_{M_L, M_S} \sum_{M_L', M_S'} \rho^{(A)}_{M_L M_S, M_L', M_S'} \times |nLSM_L M_S\rangle\langle nLSM_L' M_S'| \ . \tag{11}$$

(More detailed examples of construction of the density matrix for the target appear in Ref. [6].) In accordance with Eq. (9), the (asymptotic) system density operator for a state with projectile wave vector $\mathbf{k}$ and target state nL is just the direct product of $\hat{\rho}^{(e)}$ and $\hat{\rho}^{(A)}_{nL}$. We can construct the corresponding density matrix in either the coupled- or the uncoupled-spin representation; the diagonal elements of the resulting matrix are the relative populations in the various magnetic sublevels of the nL atomic level, while the off-diagonal elements characterize the coherence of those sublevels.

In the absence of continuum spin-orbit effects we can decompose the initial and the final spaces into eigenspaces associated with an eigenvalue of the total spin; e.g., for electron scattering from an alkali metal,

$$\mathcal{E}^{(eA)}_{nL} = {}^1\mathcal{E}^{(eA)}_{nL} \oplus {}^3\mathcal{E}^{(eA)}_{nL} \ , \tag{12}$$

where the dimensionality of each of the constituent eigenspaces is $(2\mathcal{S}+1)(2L+1)$. By writing system kets or density operators in terms of elements of these two spin eigensubspaces we can exploit the fact that the transition (8), a mapping between $\mathcal{E}^{(eA)}_{n_0 L_0}$ and $\mathcal{E}^{(eA)}_{nL}$, preserves the total spin quantum number $\mathcal{S}$ and leaves unchanged the distribution of spin eigenstates $|\mathcal{S}, \mathcal{M}_{\mathcal{S}}\rangle$ in the initial state. In analyzing experiments, however, one eventually must return to the uncoupled spin representation, since in general preparation of initial and/or analysis of final states must be described in terms of uncoupled spins, i.e., the spins of the projectile and atom separately.

The scattering operator $\hat{\mathcal{F}}(\mathbf{k}, nL \leftarrow \mathbf{k}_0, n_0 L_0)$ maps kets and density operators from $\mathcal{E}^{(eA)}_{n_0 L_0}$ to $\mathcal{E}^{(eA)}_{nL}$ as

$$|\mathbf{k}, nL\rangle = \hat{\mathcal{F}}(\mathbf{k}, nL \leftarrow \mathbf{k}_0, n_0 L_0) |\mathbf{k}_0, n_0 L_0\rangle \ , \tag{13a}$$

$$\hat{\rho}_{nL} = \hat{\mathcal{F}}(\mathbf{k}, nL \leftarrow \mathbf{k}_0, n_0 L_0) \hat{\rho}_{n_0 L_0} \hat{\mathcal{F}}(\mathbf{k}_0, n_0 L_0 \leftarrow \mathbf{k}, nL)^{\dagger} \ . \tag{13b}$$

(We have reversed the arguments of $\hat{\mathcal{F}}^{\dagger}$ as a reminder that the scattering operator takes kets from the final to the initial state space.) The matrix elements of this operator with respect to US or CS eigenkets in $\mathcal{E}^{(eA)}_{nL}$ and $\mathcal{E}^{(eA)}_{n_0 L_0}$ are just the scattering amplitudes in the corresponding representations, which in turn are proportional to the elements of the T matrix we calculate theoretically [49]:

$${}^{2\mathcal{S}+1} f_{nLSM_L \leftarrow n_0 L_0 S_0 M_{L_0}}(\theta) = \langle nLM_L; \mathcal{S}\mathcal{M}_{\mathcal{S}} | \hat{\mathcal{F}}(\mathbf{k}, nL \leftarrow \mathbf{k}_0, n_0 L_0) | n_0 L_0 M_{L_0}; \mathcal{S}\mathcal{M}_{\mathcal{S}} \rangle \tag{14a}$$

$$= -(2\pi)^2 m_e \langle nLM_L; \mathcal{S}\mathcal{M}_{\mathcal{S}} | \hat{T} | n_0 L_0 M_{L_0}; \mathcal{S}\mathcal{M}_{\mathcal{S}} \rangle \ . \tag{14b}$$

2. Density operators for experiments

To analyze experiments involving preparation of the initial state and/or analysis of the final state we require three density operators: for the initial state, for the state that results from mapping (13), and for detection or analysis of the final state. The simplest case is one in which there is no initial-state preparation, e.g., scattering of unpolarized electrons from atoms in a statistical distribution of magnetic and spin substates. Here the preparation density operator is proportional to the projection operator onto $\mathcal{E}^{(eA)}_{n_0L_0}$, the constant of proportionality being the inverse of the dimensionality of that space, as required to normalize this operator to unit trace:

$$\hat{\rho}^{(\mathrm{prep})}_{n_0L_0}=\frac{1}{4(2L_0+1)}\sum_{M_{L_0}}\sum_{\mathcal{S}\mathcal{M}_{\mathcal{S}}}|n_0L_0M_{L_0};\mathcal{S}\mathcal{M}_{\mathcal{S}}\rangle \times\langle n_0L_0M_{L_0};\mathcal{S}\mathcal{M}_{\mathcal{S}}| =\frac{1}{4(2L_0+1)}\hat{1}_{n_0L_0}\ . \tag{15}$$

Note that we can also construct the restriction of this operator to the spin eigenspace ${}^{2\mathcal{S}+1}\mathcal{E}^{(eA)}_{n_0L_0}$, which we shall need in the analysis of experiments in Sec. V, by summing only over M_{L_0} and $\mathcal{M}_{\mathcal{S}}$ and normalizing the result by the inverse of the dimensionality of that space $(2\mathcal{S}+1)(2L_0+1)$.

The density operator for the final state $\hat{\rho}_{nL}$ is constructed via Eq. (13b). Since $\hat{\mathcal{F}}(\mathbf{k},nL\leftarrow\mathbf{k}_0,n_0L_0)$ does not preserve normalization, we must explicitly normalize this density operator by dividing by its trace, if necessary. In any case, since the total spin and its projection on the axis of quantization are constants of the motion, the collision density matrix in the CS representation is diagonal in $\mathcal{S}$ and $\mathcal{M}_{\mathcal{S}}$.

Finally, the analysis density operator describes mathematically whatever monitoring of the final-state the experiment entails in addition to monitoring the energy loss and scattering angle as required for a conventional DCS measurement. For example, one might use a circularly polarized "dump" laser to select a particular final magnetic sublevel of the target. Or if, as is often the case, the detector is insufficiently sensitive to respond to a single pure state, then this operator represents the efficiency, and hence the response, of the measuring device (see Appendix D of Ref. [46]). The simplest case, of course, is an experiment with no additional analysis of the final state; in this case the (normalized) analysis density operator is just

$$\hat{\rho}^{(\mathrm{anal})}_{nL}=\frac{1}{4(2L+1)}\hat{1}_{nL}\ . \tag{16}$$

3. The detected scattering intensity

In most experiments of concern here, the essential measured quantity is the detected scattering intensity $I_{n_0L_0\rightarrow nL}(k,k_0,\theta)$. This quantity depends on the incident electron energy, the transition being studied, and the scattering angle (as well as various experimental factors such as incident beam densities) and is proportional to the squared modulus of the scattering amplitude. It is, however, more general than the conventional spin-averaged DCS, which emerges as a special case if no state preparation or analysis is performed. With the preparation and analysis density operators normalized to unit trace, the detected scattering intensity is [50]

$$I(k,k_0,\theta)=4(2L+1)\frac{k}{k_0}\mathrm{Tr}[\hat{\rho}^{(\mathrm{anal})}_{nL}\hat{\rho}_{nL}] =4(2L+1)\frac{k}{k_0}\mathrm{Tr}[\hat{\rho}^{(\mathrm{anal})}_{nL}\hat{\mathcal{F}}(\mathbf{k},nL\leftarrow\mathbf{k}_0,n_0L_0)\hat{\rho}^{(\mathrm{prep})}_{n_0L_0}\hat{\mathcal{F}}(\mathbf{k}_0,n_0L_0\leftarrow\mathbf{k},nL)^{\dagger}]\ . \tag{17}$$

To relate this intensity to the conventional spin-averaged DCS for a measurement that does not involve state preparation or analysis we evaluate the trace in the coupled spin representations, obtaining

$$\bar{\sigma}_{n_0L_0\rightarrow nL}(\theta)=\frac{1}{4(2L_0+1)}\frac{k}{k_0}\sum_{M_{L_0}}\sum_{M_L}[|{}^1f_{M_L,M_{L_0}}(\theta)|^2+3|{}^3f_{M_L,M_{L_0}}(\theta)|^2] \tag{18}$$

$$=\frac{1}{2L_0+1}\left[\frac{1}{4}{}^1\sigma_{n_0L_0\rightarrow nL}(\theta)+\left[\frac{3}{4}\right]^3\sigma_{n_0L_0\rightarrow nL}(\theta)\right]\ . \tag{19}$$

The spin-channel DCSs in (19) are the intensities (17) for each spin channel, which we can obtain by inserting the restrictions of the analysis and preparation density operators to the appropriate spin eigenspaces:

$${}^{2\mathcal{S}+1}\sigma_{n_0L_0\rightarrow nL}(\theta)=\frac{1}{2L_0+1}\frac{k}{k_0}\sum_{M_L}\sum_{M_{L_0}}|{}^{2\mathcal{S}+1}f_{M_L,M_{L_0}}(\theta)|^2\ . \tag{20}$$

The general form Eq. (17) clearly separates the details of the experiment, which are contained in $\hat{\rho}_{n_0L_0}^{(\text{prep})}$ and $\hat{\rho}_{nL}^{(\text{anal})}$, from the collision dynamics, which are described by $\hat{\mathcal{F}}(\mathbf{k},nL\leftarrow\mathbf{k}_0,n_0L_0)$.

4. *Special cases: Experiments involving either initial-state preparation or final-state analysis*

In most experimental studies of this problem to date, *either* the initial state is not prepared or the final state is not analyzed. In the absence of state preparation the initial-state density operator Eq. (15) represents the mixed state defined by the appropriate equilibrium statistical distribution of eigenstates in $\mathcal{E}_{n_0L_0}^{(eA)}$. In the case of these "coincidence experiments" we can usefully define a collision operator

$$\hat{\sigma}_{nL}\equiv\hat{\mathcal{F}}(\mathbf{k},nL\leftarrow\mathbf{k}_0,n_0L_0)\hat{\mathcal{F}}(\mathbf{k}_0,n_0L_0\leftarrow\mathbf{k},nL)^{\dagger}, \quad (21)$$

and write the detected intensity (17) as

$$I_{n_0L_0\rightarrow nL}(k,k_0,\theta)=\frac{2L+1}{2L_0+1}\frac{k}{k_0}\text{Tr}[\hat{\rho}_{nL}^{(\text{anal})}\hat{\sigma}_{nL}] . \quad (22)$$

The second special case allows for initial-state preparation but not final-state analysis, as in the experiments to be discussed in Sec. V. Here the analysis density matrix is given by Eq. (16). If we cyclically permute the remaining operators in the detected scattering intensity we can define a collision operator analogous to that of Eq. (21),

$$\hat{\sigma}_{n_0L_0}\equiv\hat{\mathcal{F}}(\mathbf{k}_0,n_0L_0\leftarrow\mathbf{k},nL)^{\dagger}\hat{\mathcal{F}}(\mathbf{k},nL\leftarrow\mathbf{k}_0,n_0L_0) , \quad (23)$$

and write the detected scattering intensity for these "pumped-target" experiments as

$$I_{n_0L_0\rightarrow nL}(k,k_0,\theta)=\frac{k}{k_0}\text{Tr}[\hat{\rho}_{n_0L_0}^{(\text{prep})}\hat{\sigma}_{n_0L_0}] . \quad (24)$$

We shall analyze experiments of each type in Sec. III and compare to data from them in Sec. V.

C. Relationship between inelastic and superelastic scattering experiments

Direct measurement of DCSs or orientation and alignment parameters (e.g., by measuring the scattered electron in coincidence with a fluorescence photon from the excited atom) is not the only route to information about inelastic scattering from the ground state. As argued by MacGillivray and Standage [48,50] and first realized in the experiments of Hermann, Hertel, and Kelley [4,5] and of McClelland, Kelley, and Celotta [8,9], the principle of microreversability [51] relates the scattering amplitudes for direct excitation and the time-reversed experiment, superelastic deexcitation. On the one hand, one can perform a direct measurement of (unpolarized) electron-induced $3s\rightarrow 3p$ transitions in, say, the coincidence experiment

$$e(\mathbf{k}_0)+\text{Na}(3\,^2S_{1/2})\rightarrow e(\mathbf{k},m_s)+\text{Na}(3\,^2P_J,M_J) , \quad (25)$$

with detection of the spin of the outgoing electron and/or the final state of the atom (e.g., by analyzing the fluorescence photon emitted in spontaneous emission from the $3\,^2P_J$ state). Alternatively, one can access precisely the same information in the time-reversed superelastic experiment

$$e(-\mathbf{k},m_s)+\text{Na}(3\,^2P_J,M_J)\rightarrow e(-\mathbf{k}_0)+\text{Na}(3\,^2S_{1/2}) , \quad (26)$$

where the incident electron beam is spin polarized and the incident atomic beam is prepared in an excited state with a well-defined nonequilibrium distribution among its magnetic sublevels. If the spins of the superelastically scattered electrons are detected, then the corresponding inelastic experiment Eq. (25) would involve spin-polarized incoming electrons.

Time-reversal invariance relates the scattering information from these inelastic and superelastic scattering events. To clarify this relationship, McClelland, Kelley, and Celotta define the natural frame, with respect to which spatial quantization is declared, using the initial-state wave vectors of the *superelastic* collision in Eq. (26) rather than those of the inelastic collision in Eq. (25) as in Fig. 1(b). If we temporarily denote the incoming and the outgoing electron wave vectors in the inelastic process (25) by $\mathbf{k}_0^{s\rightarrow p}$ and $\mathbf{k}^{s\rightarrow p}$, then as shown in (26) and illustrated in Fig. 1(b), we can write the incoming and the outgoing wave vectors for the superelastic process as

$$\begin{aligned}\mathbf{k}_0^{p\rightarrow s}&=-\mathbf{k}^{s\rightarrow p} ,\\ \mathbf{k}^{p\rightarrow s}&=-\mathbf{k}_0^{s\rightarrow p} .\end{aligned} \quad (27)$$

Then we can rewrite the definition of the z and x axes of the natural frame in terms of wave vectors appropriate to the superelastic event as

$$\begin{aligned}\hat{z}^{n}&=\mathbf{k}_0^{s\rightarrow p}\times\mathbf{k}^{s\rightarrow p}=-(\mathbf{k}_0^{p\rightarrow s}\times\mathbf{k}^{p\rightarrow s}) ,\\ \hat{x}^{n}&=\mathbf{k}_0^{s\rightarrow p}=-\mathbf{k}^{p\rightarrow s} .\end{aligned} \quad (28)$$

In this frame, the inelastic and the superelastic scattering amplitudes are complex conjugates of one another. So the density operators for the final states produced in the two processes are identical. Preparation of the initial state for the superelastic experiment is represented by a preparation density operator identical to $\hat{\rho}_{nL}^{(\text{anal})}$ for the time-reversed inelastic experiment.

D. Orientation and alignment parameters

Actually performing a complete experiment [33–37], i.e., determining all accessible information in the amplitudes for a particular scattering event, poses a pragmatic challenge to the experimentalist: which independent parameters are most easily measured? As first discussed by Bederson [33–37], these parameters should be amenable to easy physical interpretation and should characterize the dynamics irrespective of the details of state preparation or analysis. For $s\leftrightarrow s$ and $s\leftrightarrow p$ transitions in e-Na scattering, this question has been addressed by Andersen and Bartschat [52]. In this section we shall review the parameter set they proposed as implemented in measurements by McClelland and co-workers [8–15] (see Sec. V) in light of the above formalism and relate them to the CS scattering amplitudes.

1. The triplet-singlet ratio and the exchange asymmetry

Two parameters are common to both the $s \rightarrow s$ and $s \rightarrow p$ transitions: the spin-averaged DCS and the ratio of DCSs for scattering in the triplet and the singlet spin channels. The first of these is the most familiar: the absolute spin-averaged DCS $\overline{\sigma}_{n_0L_0 \rightarrow nL}(\theta)$ of Eq. (19) describes scattering in the absence of initial-state preparation or final-state analysis (e.g., of unpolarized electrons from atoms in a statistical distribution of magnetic sublevels). The triplet-to-singlet ratio, which quantifies the relative strength of scattering into these two spin channels, is defined as

$$r(\theta)=\frac{\sum_{M_L} |{}^3f_{M_L,M_{L_0}}(\theta)|^2}{\sum_{M_L} |{}^1f_{M_L,M_{L_0}}(\theta)|^2} . \tag{29}$$

A parameter that is physically equivalent to the triplet-to-singlet ratio and offers some experimental advantages is the *exchange asymmetry* (also known as the spin asymmetry) $A_{M_L}^{(\mathrm{ex})}(\theta)$ for scattering into sublevel M_L of the final state [24,25]. Operationally, the exchange asymmetry is defined in terms of detected intensities for collisions of spin-polarized electrons from spin-polarized atoms that leave the atoms in specific magnetic sublevels M_L of the nL final state. In particular, $A_{M_L}^{(\mathrm{ex})}(\theta)$ is proportional to the difference between the intensity $I_{M_L}^{\mathrm{para}}(\theta)$ for scattering with parallel electron and atomic spins and $I_{M_L}^{\mathrm{anti}}(\theta)$ for antiparallel spins. This difference is normalized by dividing by the sum of these intensities and, if the polarization of the incident beams is not perfect, by the initial degrees of polarization of the incident electrons and/or atoms. If, as in the experiments of McClelland and co-workers, the degree of polarization of the incident electrons is P_e and that of the atoms is P_a, then the appropriate operational definition is

$$A_{M_L}^{(\mathrm{ex})}(\theta) \equiv \frac{1}{|P_A P_e|} \frac{I_{M_L}^{\mathrm{anti}}(\theta)-I_{M_L}^{\mathrm{para}}(\theta)}{I_{M_L}^{\mathrm{anti}}(\theta)+I_{M_L}^{\mathrm{para}}(\theta)} . \tag{30}$$

In experiments that do not specify the final magnetic sublevel, the measured quantity is an averaged exchange asymmetry, which is related to the triplet-singlet ratio by

$$\overline{A}^{(\mathrm{ex})}(\theta) \equiv \frac{1-r_{n_0L_0 \rightarrow nL}(\theta)}{1+3r_{n_0L_0 \rightarrow nL}(\theta)} . \tag{31}$$

Experimentally, the exchange asymmetry is particularly attractive because as a ratio of intensities it is insensitive to absolute intensity calibrations. Its value is delimited by $-\frac{1}{3}$ (pure triplet scattering) and $+1$ (pure singlet scattering).

2. The triplet-singlet phase angle

The spin-averaged DCS and triplet-singlet ratio (or, equivalently, the exchange asymmetry) contain information about the magnitudes of the singlet and the triplet amplitudes. The next parameter complements this with information about their phases. For a transition from initial state $(n_0L_0M_{L_0})$ to final state (nLM_L), the triplet-singlet phase angle is defined in terms of the real and the imaginary parts of the (nonzero) natural-frame amplitudes as

$$\Delta_{M_L,M_{L_0}}(\theta) \equiv \arg[{}^3f_{M_L,M_{L_0}}(\theta)] - \arg[{}^1f_{M_L,M_{L_0}}(\theta)] . \tag{32}$$

For an $s \rightarrow s$ transition such as elastic scattering, there is only one such angle, for $M_L = M_{L_0} = 0$. A complete description of a $s \rightarrow s$ transition, then, is contained in the three real parameters

$$\{\overline{\sigma}_{n_0s \rightarrow ns}(\theta), r_{n_0s \rightarrow ns}(\theta), \Delta_{0,0}(\theta)\} . \tag{33}$$

3. Scattering to a non-s state: The angular-momentum transfer

If the initial state is an s state and the final state is not an s state (i.e., if $L > 0$), then we require more than three independent real parameters to fully describe a scattering event. In such collisions orbital angular momentum is transferred from the projectile to the target [52] and further information about scattering is contained in $L_{n_0L_0 \rightarrow nL}^{(\perp)}(\theta)$, the mean angular momentum transferred to the atom normal to the scattering plane as a consequence of the collision. This parameter is especially appealing because of its clear physical interpretation. In the natural frame we can write the expectation value of the projection of the valence electron's orbital angular momentum along an axis normal to the scattering plane in terms of the density matrix of the final state as

$$\overline{L}_{n_0L_0 \rightarrow nL}^{(\perp)}(\theta) \equiv \langle \hat{L}_z \rangle_{nL} = \frac{\mathrm{Tr}[\hat{L}_z \hat{\rho}_{nL}]}{\mathrm{Tr}[\hat{\rho}_{nL}]} . \tag{34}$$

As the overbar implies, this expression yields an average angular-momentum transfer $\overline{L}_{n_0L_0 \rightarrow nL}^{(\perp)}(\theta)$.

In each of these $(2\mathcal{S}+1)(2L+1)$-dimensional eigenspaces, we obtain for an arbitrary transition and experiment the spin-channel angular-momentum transfer

$$ {}^{2\mathcal{S}+1}L_{n_0L_0 \rightarrow nL}^{(\perp)}(\theta) = \frac{(2\mathcal{S}+1)}{\mathrm{Tr}[{}^{2\mathcal{S}+1}\hat{\rho}_{nL}]} \times \sum_{M_L} M_L \langle nLM_L;\mathcal{S}\mathcal{M}_{\mathcal{S}}|{}^{2\mathcal{S}+1}\hat{\rho}_{nL}|nLM_L;\mathcal{S}\mathcal{M}_{\mathcal{S}}\rangle , \tag{35}$$

which is the sum of the projections of the final-state orbital angular momentum weighted by the diagonal elements of the density matrix, the relative populations of finding the final state in each magnetic sublevel. In the

special case of experiments in which no initial-state preparation is performed, we can write this expression in terms of the spin-channel DCS (20) as

$$ {}^{2\mathcal{S}+1}L^{(\perp)}_{n_0L_0\to nL}(\theta)=\frac{1}{2L_0+1}\frac{k}{k_0}\left[\frac{1}{{}^{2\mathcal{S}+1}\sigma_{n_0L_0\to nL}(\theta)}\right]\times\sum_{M_L}M_L\sum_{M_{L_0}}|{}^{2\mathcal{S}+1}f_{M_L,M_{L_0}}(\theta)|^2 . \tag{36}$$

For example, for an $s\to p$ transition, with one unit of angular momentum transferred to the target along $\hat{z}^n$, the (natural-frame) amplitudes for $M_L=\pm1$ are nonzero. If the initial state is not prepared, then Eq. (36) reveals the angular-momentum transfer to be proportional to the difference between these amplitudes:

$$ {}^{2\mathcal{S}+1}L^{(\perp)}_{3s\to3p}(\theta)=\frac{|{}^{2\mathcal{S}+1}f_{+1,0}(\theta)|^2-|{}^{2\mathcal{S}+1}f_{-1,0}(\theta)|^2}{|{}^{2\mathcal{S}+1}f_{+1,0}(\theta)|^2+|{}^{2\mathcal{S}+1}f_{-1,0}(\theta)|^2} \tag{37a}$$

$$ =\frac{k}{k_0}\frac{1}{{}^{2\mathcal{S}+1}\sigma_{3s\to3p}(\theta)}\times[|{}^{2\mathcal{S}+1}f_{+1,0}(\theta)|^2-|{}^{2\mathcal{S}+1}f_{-1,0}(\theta)|^2] . \tag{37b}$$

In this case, then, the angular-momentum transfer in spin channel $2\mathcal{S}+1$ is proportional to the difference between the diagonal density-matrix elements, i.e., the relative probabilities for finding the atom in a final state in which the projection of the orbital angular momentum of the valence electron along $\hat{z}^n$ is M_L. This contrasts strikingly with the DCS for spin channel $\mathcal{S}$, Eq. (20), which is proportional to the sum of these elements.

4. *Singlet and triplet alignment angles*

The other elements of the final-state density matrix—the off-diagonal elements—contain information about the final state of the valence electron, a state that is "created" by electron scattering at angle θ. In terms of the scattering amplitude, these elements have the form ${}^{2\mathcal{S}+1}f_{M_L,M_{L_0}}(\theta)^{*\,2\mathcal{S}+1}f_{M'_L,M'_{L_0}}(\theta)$ and depend on the phase relationships between amplitudes for different magnetic substates; we can use them to define additional OA parameters, the alignment (or symmetry) angles. For an $s\to p$ transition there is only one unique off-diagonal element, and we can define the relative phase angle γ *between the amplitudes for* $M_L=-1$ *and* $+1$ *in spin-channel* $2\mathcal{S}+1$ in terms of the corresponding amplitudes as

$$ {}^{2\mathcal{S}+1}f_{-1,0}(\theta)^{*\,2\mathcal{S}+1}f_{+1,0}(\theta)\equiv-|{}^{2\mathcal{S}+1}f_{+1}(\theta)|\,|{}^{2\mathcal{S}+1}f_{-1}(\theta)|e^{-2i\gamma} , \tag{38}$$

where γ depends implicitly on the transition and on the total spin $\mathcal{S}$. Although γ, like other OA parameters, characterizes the final state of the valence electron, it is intrinsically a two-electron quantity, "controlled" by the probability amplitudes for electron scattering at angle θ.

The physical meaning of these angles becomes clear if we relate them to the system wave function $\Psi_{\mathbf{k}_0,m_{s_0},\alpha_0}(\tau_e,\mathbf{r},\sigma)$ of Eq. (2), more precisely, to the part of this wave function that describes the dependence of the scattered wave on the angular coordinates of the valence electron θ_v,ϕ_v. We shall consider a pure final atomic p state, i.e., a coherent superposition of (natural-frame) angular-momentum eigenstates $|n1M_L\rangle$ for $M_L=-1,0,+1$ with coefficients given for electron scattering angle θ by the amplitudes ${}^{2\mathcal{S}+1}f_{M_L,0}(\theta)$.

Since in the natural frame the electron cannot excite the $M_L=0$ sublevel, the angular dependence of the wave function $\psi_v(\mathbf{r}_v)$ of the valence electron (with coordinates $\mathbf{r}_v$ in the natural frame) is comprised of the spherical harmonics $Y_1^{+1}(\theta_v,\phi_v)$ and $Y_1^{-1}(\theta_v,\phi_v)$. (Recall that in the natural frame the scattering angle θ does not coincide with the polar angle θ_v.) We now reexpress the boundary conditions (2) in the coupled-spin representation, where the wave function in a particular spin channel is ${}^{2\mathcal{S}+1}\Psi_{\mathbf{k}_0,n_0,L_0,M_{L_0}}(\tau_e,\mathbf{r},\sigma)$, so as to introduce the spin-channel amplitudes (5). From the scattered-wave term in the resulting boundary conditions we can separate out a factor $\psi_{\mathbf{k},n,L}(\theta_v,\phi_v,\theta)$ that describes the dependence of this wave function (in spin channel $2\mathcal{S}+1$) on the angular variables of the scattered and valence electrons, viz.,

$$ \psi_{\mathbf{k},n,L}(\theta_v,\phi_v,\theta)=\sum_{M_L}{}^{2\mathcal{S}+1}f_{M_L,M_{L_0}}(\theta)Y_L^{M_L}(\theta_v,\phi_v) , \tag{39}$$

where for the np state the amplitudes for $M_L=0$ are zero. The squared modulus of this function is proportional to the probability for finding the valence electron anywhere along a "ray" defined by the valence angles θ_v,ϕ_v; it therefore reflects the "shape" of the excited state.

In the scattering plane, where $\theta_v=\pi/2$, (39) depends only on the (natural-frame) azimuthal angle ϕ_v of the valence electron and, of course, on the projectile (scattering) angle θ:

$$ \psi_{\mathbf{k},n,L}(\theta_v=\pi/2,\phi_v,\theta)=\left[\frac{3}{8\pi}\right]^{1/2}[{}^{2\mathcal{S}+1}f_{-1,0}(\theta)e^{-i\phi_v}+{}^{2\mathcal{S}+1}f_{+1,0}(\theta)e^{+i\phi_v}] . \tag{40}$$

Using the definition (38) of the alignment angles, we can write the (unnormalized) probability for simultaneous detection of the scattering and valence electrons at this angle as

$$ |\psi_{\mathbf{k},n;L}(\theta_v=\pi/2,\phi_v,\theta)|^2=|{}^{2\mathcal{S}+1}f_{-1}(\theta)|^2+|{}^{2\mathcal{S}+1}f_{+1}(\theta)|^2+2|{}^{2\mathcal{S}+1}f_{-1}(\theta)||{}^{2\mathcal{S}+1}f_{+1}(\theta)|\cos[2(\phi_v-\gamma)] . \tag{41}$$

This probability attains its maximum for azimuthal angle

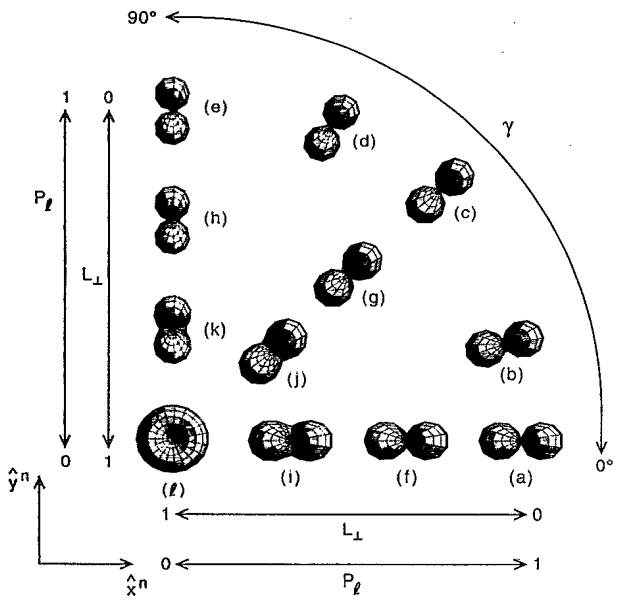

FIG. 2. Angular variation of the charge distribution of a $3p$ Na valence electron for various values of the orientation and alignment parameters in the scattering plane of the natural frame. The subfigures correspond to entries in Table I.

$\phi_v = \gamma$. Therefore γ can be interpreted as an "alignment angle" that relates the symmetry axis of the valence electron p-state charge cloud to the $\hat{x}^n$ axis of the natural frame.

For an $s \rightarrow p$ transition, ${}^{2\mathcal{S}+1}L^{(\perp)}(\theta)$ for $M_L = \pm 1$ and the alignment angles ${}^1\gamma$ and ${}^3\gamma$ characterize the shape and orientation of the wave function of the $3p$ valence electron in the scattering plane. Table I gives the values of these real parameters for $3p$ valence-electron wave functions whose angular probability densities are shown in Fig. 2, i.e., for various values of the scattering amplitudes $f_{M_L,0}(\theta)$ that describe the admixture of orbital angular momentum eigenstates $|nLM_L\rangle$ in the final state [see Eq. (40)].

5. *A complete $s \rightarrow p$ scattering experiment*

As we have seen, to fully characterize the four complex scattering amplitudes ${}^{2\mathcal{S}+1}f_{\pm 1,0}(\theta)$ of an $s \rightarrow p$ transition we require seven independent parameters. The first two, the absolute spin-averaged DCS (19) and the triplet-to-singlet ratio (29), are physically analogous to those for an $s \rightarrow s$ transition. The second two, ${}^{2\mathcal{S}+1}L^{(\perp)}_{s\rightarrow p}(\theta)$ for $2\mathcal{S}+1=1,3$, quantify for each spin channel the difference between scattering into the $M_L = +1$ and -1 substates of

TABLE I. Orientation and alignment parameters corresponding to the p wave functions in Fig. 2. The first column associates each row of the table with an entry in the figure. The a_{M_L} are the weights of the $M_L = \pm 1$ eigensubstates in Eq. (39). The $a_{\pm 1}$ are alternate expansion coefficients of the angular eigenstates in Eq. (39). Unlike the coefficients $f_{M_L=\pm 1, M_{L_0}=0}$, which normalize the wave function so it is proportional to the differential cross section, these coefficients normalize the wave function to 1. The angular-momentum transfer $L_\perp$ and the alignment angle γ are defined in Sec. II D and the linear polarization $P^{(\text{lin})}$ in Sec. III B.

Fig. 2	a_{+1}	a_{-1}	$L^\perp$	P^{lin}_{np}	γ
a	$\frac{-1}{\sqrt{2}}$	$\frac{1}{\sqrt{2}}$	0	1	0°
b	$\frac{-\sqrt{3}+i}{\sqrt{8}}$	$\frac{\sqrt{3}+1}{\sqrt{8}}$	0	1	30°
c	$\frac{-1+i}{2}$	$\frac{1+i}{2}$	0	1	45°
d	$\frac{-1+\sqrt{3}i}{\sqrt{8}}$	$\frac{1+\sqrt{3}i}{\sqrt{8}}$	0	1	60°
e	$\frac{i}{\sqrt{2}}$	$\frac{i}{\sqrt{2}}$	0	1	90°
f	$-\sqrt{\frac{2}{3}}$	$\sqrt{\frac{1}{3}}$	$\frac{1}{3}$	$\frac{2\sqrt{2}}{3}$	0°
g	$\frac{-1+i}{\sqrt{3}}$	$\frac{1+i}{\sqrt{6}}$	$\frac{1}{3}$	$\frac{2\sqrt{2}}{3}$	45°
h	$\sqrt{\frac{2}{3}}i$	$\sqrt{\frac{1}{3}}i$	$\frac{1}{3}$	$\frac{2\sqrt{2}}{3}$	90°
i	$-\sqrt{\frac{5}{6}}$	$\sqrt{\frac{1}{6}}$	$\frac{2}{3}$	$\frac{\sqrt{5}}{3}$	0°
j	$\sqrt{\frac{5}{12}}(-1+i)$	$\frac{1+i}{\sqrt{12}}$	$\frac{2}{3}$	$\frac{\sqrt{5}}{3}$	45°
k	$\sqrt{\frac{5}{6}}i$	$\sqrt{\frac{1}{6}}i$	$\frac{2}{3}$	$\frac{\sqrt{5}}{3}$	90°
l	1	0	1	0	[a]

[a]The $M_L = \pm 1$ eigenstates are circular in the xy plane of the natural frame, so γ is undefined.

the final p state.

The information obtained by measuring these four parameters is equivalent to that in the magnitude of the $s \rightarrow p$ scattering amplitudes. To complete this description of the collision we require three relative phase angles. The alignment angles describe the phase difference between the $M_L = +1$ and -1 amplitudes in each spin channel, while the triplet-singlet phase angles $\Delta_{\pm 1}(\theta)$ describe the phase difference between amplitudes with the same M_L for different spin channels. These four angles are not, however, independent, and we follow Refs. [52,27,6] in choosing $\Delta_{+1,0}(\theta)$ as the seventh independent parameter. The complete set of $s \rightarrow p$ parameters is therefore

$$\{\bar{\sigma}_{s\rightarrow p}(\theta), r_{s\rightarrow p}(\theta), {}^1L^{(\perp)}_{s\rightarrow p}(\theta), {}^3L^{(\perp)}_{s\rightarrow p}(\theta), {}^1\gamma_{s\rightarrow p}(\theta), {}^3\gamma_{s\rightarrow p}(\theta), \Delta_{+1,0}(\theta)\} \ . \tag{42}$$

III. THEORY: DESCRIPTION OF PARADIGMATIC EXPERIMENTS

To illustrate application of the formulation described in the preceding section and to describe the experiments that produced the results to which we shall compare in Sec. V, we here briefly consider three paradigmatic kinds of experiments. The first, which were performed for e-Na scattering by McClelland, Kelley, and Celotta [8,9], involve preparation of the initial state of the electrons and atoms but no final-state analysis. The second, which are conventional coincidence experiments, entail the reverse special case: no state preparation but final-state analysis through detection of the polarization of photons emitted when the atom that was excited by electron impact subsequently decays. The third, which have been performed by Hegemann *et al.* [17], entail *both* preparation of the initial state and analysis of the final state of the electrons.

A. Experiments with initial-state preparation only: Scattering of spin-polarized electrons from spin-polarized atoms

In a series of papers [8,9,11,13,15], McClelland and co-workers have measured spin-dependent cross sections and OA parameters for elastic ($3s \rightarrow 3s$) and superelastic ($3p \rightarrow 3s$) scattering of beams of spin-polarized electrons from beams of state-selected Na atoms in order to resolve scattering in the singlet and the triplet spin channels. Of particular interest here are experiments that use optical pumping to spin polarize the initial atoms along the $\hat{z}^n$ axis of the natural frame, normal to the scattering plane. (The electron beam is spin polarized along the same axis.) No final-state analysis was performed, so these experiments conform to the case of Eq. (16), for which the collision operator and detected intensity are given by Eqs. (23) and (24). By applying time-reversal invariance to the superelastic ($3p \rightarrow 3s$) data they obtain the OA parameters for inelastic ($3s \rightarrow 3p$) scattering to which we compare below. For elastic scattering McClelland and coworkers have published data for the triplet-to-singlet ratio $r(\theta)$ and (equivalently) the exchange asymmetry $A_0^{(\mathrm{ex})}(\theta)$ at 1.0, 1.6, and 4.1 eV. By combining these data with results from other elastic experiments, they published a nearly complete determination of the scattering amplitude, lacking only the sign of the triplet-singlet phase angle $\Delta_{0,0}(\theta)$.

Description of these experiments in terms of density operators is especially simple. The electron beam is spin polarized along $\hat{z}^n$ with degree of polarization $|P_0| = 0.32 \pm 0.02$, so for this (mixed) state the electron density operator in $\mathcal{E}^{(e)}$ is

$$\hat{\rho}^{(e)} = \tfrac{1}{2}[(1+P_0)|+\tfrac{1}{2}\rangle\langle+\tfrac{1}{2}| + (1-P_0)|-\tfrac{1}{2}\rangle\langle-\tfrac{1}{2}|] \ . \tag{43}$$

By inserting $P_0 = \pm|P_0|$ we can use this operator to describe either spin-up or spin-down polarization.

The atomic beam is also spin polarized along $\hat{z}^n$, the atoms having been prepared via two-step optical pumping using circularly polarized laser light. The resulting initial state of the target atoms is a pure state, one of the two $M_F = \pm F$ hyperfine levels of the ground state of Na. For these particular hyperfine levels, the sign of the atomic spin projection $M_S = \pm\frac{1}{2}$ along $\hat{z}^n$ (and, for a $3p$ initial state, the sign of $M_L = \pm 1$) is the same as that of M_F. So the appropriate atomic density operator in $\mathcal{E}^{(A)}_{3s}$ is

$$\hat{\rho}^{(A)}_{n_0L_0} = |n_0L_0M_{L_0}M_{S_0}\rangle\langle n_0L_0M_{L_0}M_{S_0}| \ . \tag{44}$$

We can now construct the preparation density operator in the UC representation as

$$\hat{\rho}^{(\mathrm{prep})}_{n_0L_0}(M_{S_0}, M_{L_0}) = \sum_{m_{s_0}} (\tfrac{1}{2} + m_{s_0}P_0) \times |m_{s_0}, n_0L_0M_{L_0}M_{S_0}\rangle\langle m_{s_0}, n_0L_0M_{L_0}M_{S_0}| \tag{45a}$$

or, using the Clebsch-Gordan series (3), in the CS representation as

$$\hat{\rho}^{(\mathrm{prep})}_{n_0L_0}(M_{S_0}, M_{L_0}) = \sum_{m_{s_0}} (\tfrac{1}{2} + m_{s_0}P_0) \times \sum_{\mathcal{S},\mathcal{S}'} C(\tfrac{1}{2}\tfrac{1}{2}\mathcal{S}; m_{s_0}M_{S_0}) C(\tfrac{1}{2}\tfrac{1}{2}\mathcal{S}'; m_{s_0}M_{S_0}) \times |n_0L_0M_{L_0}; \mathcal{S}\mathcal{M}_{\mathcal{S}}\rangle\langle n_0L_0M_{L_0}; \mathcal{S}'\mathcal{M}_{\mathcal{S}}| \ , \tag{45b}$$

where we have explicitly noted the projection quantum numbers specified by initial-state preparation.

For each of the four possible experiments one can perform with this setup ($P_0=\pm|P_0|$ and $M_S=\pm\frac{1}{2}$ with, for a $3p$ initial state, $M_L=\pm1$), the construction of the detected scattering intensity (24) is especially simple since the collision operator (23) is diagonal with respect to $\mathcal{S}$ and independent of $\mathcal{M}_\mathcal{S}$. The CS matrix elements of the collision operator are

$$\langle n_0L_0M_{L_0};\mathcal{S}\mathcal{M}_\mathcal{S}|\hat{\sigma}_{n_0L_0}|n_0L_0M'_{L_0};\mathcal{S}\mathcal{M}_\mathcal{S}\rangle = \sum_{M_L} {}^{2\mathcal{S}+1}f_{M_L,M_{L_0}}(\theta)\,{}^{2\mathcal{S}+1}f_{M_L,M'_{L_0}}(\theta)^* \ . \quad (46)$$

The matrix elements of $\hat{\rho}^{(\mathrm{prep})}_{n_0L_0}$ are also diagonal in $\mathcal{S}$, $\mathcal{M}_\mathcal{S}$, and M_{L_0} and for a particular M_{S_0}, are nonzero only if

$$\mathcal{M}_\mathcal{S}=m_{s_0}+M_{S_0}=m_s+M_S \ . \quad (47)$$

Using this fact we evaluate the trace in Eq. (24) to obtain for the detected scattering intensity

$$I_{n_0L_0\to nL}(k,k_0,\theta) = \frac{k}{k_0}\sum_\mathcal{S} |{}^{2\mathcal{S}+1}f_{M_{L_0},M_{L_0}}(\theta)|^2 \times \sum_{m_{s_0}} (\tfrac{1}{2}+m_{s_0}P_0)[C(\tfrac{1}{2}\tfrac{1}{2}\mathcal{S};m_{s_0}M_{S_0})]^2 \ . \quad (48)$$

To determine the exchange asymmetry $A^{(\mathrm{ex})}_{M_L}(\theta)$ for either the elastic or the superelastic experiments we need only construct the parallel and antiparallel intensities in Eq. (30). The two are distinguished by the sign of $M_{S_0}=\pm\frac{1}{2}$, so we can write the intensity Eq. (48) for both configurations as

$$I_{3L_0\to 3L}(k,k_0,\theta)=\tfrac{1}{4}[(1-2M_{S_0}P_0)|{}^1f_{M_{L_0},M_{L_0}}(\theta)|^2 + (3+2M_{S_0}P_0)|{}^3f_{M_{L_0},M_{L_0}}(\theta)|^2] \ . \quad (49)$$

For elastic scattering, for which $M_L=0$ only, we must multiply this result by 2 to construct the measured intensities because there are two parallel and two antiparallel configurations: e.g., we get antiparallel intensities for $M_{S_0}=+\frac{1}{2}$ and $P_0=-|P_0|$ and for $M_{S_0}=-\frac{1}{2}$ and $P_0=+|P_0|$. For the superelastic case, with $M_L=\pm1$, the sign of $M_{S_0}=\pm\frac{1}{2}$ follows that of M_{L_0}, so there is only one parallel and one antiparallel configuration for each M_L.

For elastic scattering, we can extract the triplet-to-singlet ratio (or, equivalently, the exchange asymmetry) from this experiment. The superelastic experiment allows us to determine the triplet-to-singlet ratio and the spin-selected angular momentum transfers ${}^{2\mathcal{S}+1}L^{(1)}_{3p\to3s}(\theta)$. Data from this experiment can further be manipulated to yield the exchange asymmetries $A^{(\mathrm{ex})}_{M_L}(\theta)$.

For either transition we can construct this quantity from the operational definition (30). For elastic scattering the results involves the spin-averaged DCS (19)

$$A^{(\mathrm{ex})}_0(\theta)=\frac{1}{4P_0}\frac{k}{k_0}\frac{|{}^1f_{0,0}(\theta)|^2-|{}^3f_{0,0}(\theta)|^2}{\bar{\sigma}_{3s\to3s}(\theta)} \ , \quad (50)$$

while for superelastic scattering we obtain

$$A^{(\mathrm{ex})}_{M_{L_0}}(\theta)=\frac{1}{P_0}\frac{|{}^1f_{M_{L_0},0}(\theta)|^2-|{}^3f_{M_{L_0},0}(\theta)|^2}{|{}^1f_{M_{L_0},0}(\theta)|^2+3|{}^3f_{M_{L_0},0}(\theta)|^2} \quad (M_{L_0}=\pm1) \ . \quad (51)$$

B. Experiments with final-state analysis only: Coincidence experiments

The most widely used procedure for experimentally probing the dynamics of electron-atom collisions beyond the conventional DCS is a coincidence experiment. Using crossed electron and atomic beams with no initial-state preparation, such experiments gain insight into the nature of the final atomic state created by electron-impact excitation $n_0L_0\to nL$ at fixed scattering angle by measuring the polarization of the radiation emitted when the excited atom undergoes the subsequent decay $nL\to n_fL_f$. The quantity thus introduced $P^{(\mathrm{lin})}_{nL}(\theta)$ is a measure of the linear polarization in the scattering plane of light emitted normal to that plane—information that complements that provided by $L^{(1)}_{nL}(\theta)$ concerning the degree of circular polarization of the emitted photon. (For an $s\to p$ excitation in which the spin is resolved, these quantities are not independent.) In practice, $P^{(\mathrm{lin})}_{nL}(\theta)$ is determined using a photon detector oriented normal to the scattering plane (along $\hat{z}^n$ of the natural frame) that detects linearly polarized photons whose polarization vector (in the scattering plane) defines an (azimuthal) angle β with $\hat{x}^n$.

Operationally, the linear polarization is defined in terms of the intensity of this linearly polarized light for electron scattering angle θ and polarization angle β, $I_{nL\to n_fL_f}(\beta,\theta)$. Specifically, $P^{(\mathrm{lin})}_{nL}(\theta)$ is the difference between maximum and minimum values of this intensity, normalized as usual by the sum of these two values. If, for example, the decay is from a final $3p$ to a $3s$ state, then we require values at the polarization angles β of the maximum and minimum intensity for a (pure) p state, which we can express in terms of the alignment angle γ defined in Eq. (38). In the natural frame, such a state radiates like a classical dipole in the scattering plane, so the radiated intensity attains its minimum at $\beta=\gamma$ and its maximum at $\beta=\gamma+\pi/2$.

To evaluate the detected scattering intensity (22) for experiments with final-state analysis but no initial-state preparation, we require the collision operator (21), which in this case is just the final-state density operator $\hat{\rho}_{nL}$, and the analysis density operator, which is the photon polarization detection operator. We can write matrix elements of the collision operator in the CS representation, which is algebraically most convenient, as simple sums of CS scattering amplitudes over the initial eigenkets in $\mathcal{C}^{(eA)}_{n_0L_0}$,

$$\langle nLM_L;\mathcal{SM}_\mathcal{S}|\hat{\sigma}_{nL}|nLM'_L;\mathcal{SM}_\mathcal{S}\rangle = \sum_{M_{L_0}} {}^{2\mathcal{S}+1}f_{M_L,M_{L_0}}(\theta)\,{}^{2\mathcal{S}+1}f_{M'_L,M_{L_0}}(\theta)^* \ . \quad (52)$$

We can write the photon detection operator $D_{n_fL_f}(\beta)$ for a decay transition $nL\rightarrow n_fL_f$ in terms of the spatial coordinates $\mathbf{r}_v$ of the valence electron and the polarization vector $\hat{\epsilon}$ in the CS basis as

$$\hat{\rho}_{nL}^{(\text{anal})}=D_{n_fL_f}(\beta)\equiv \sum_{\mathcal{SM}_\mathcal{S}}\sum_{M_{L_f}} (\hat{\epsilon}\cdot\mathbf{r}_v)|n_fL_fM_{L_f};\mathcal{SM}_\mathcal{S}\rangle \times\langle n_fL_fM_{L_f};\mathcal{SM}_\mathcal{S}|(\hat{\epsilon}^*\cdot\mathbf{r}_v) \ . \quad (53)$$

The detected intensity is the sum of singlet and triplet contributions. For each we evaluate the trace in Eq. (22) in ${}^{2\mathcal{S}+1}\mathcal{E}_{nL}^{(eA)}$ and exploit the fact that the analysis density operator (53) is diagonal with respect to $\mathcal{M}_\mathcal{S}$, obtaining

$$I_{nL\rightarrow n_fL_f}(\beta,\theta)=\frac{2L+1}{2L_0+1}\left[\frac{k}{k_0}\right]\sum_{\mathcal{S}}(2\mathcal{S}+1)\sum_{M_L,M'_L}\sum_{M_{L_f}}\langle nLM'_L|(\hat{\epsilon}\cdot\mathbf{r}_v)|n_fL_fM_{L_f}\rangle\langle n_fL_fM_{L_f}|(\hat{\epsilon}^*\cdot\mathbf{r}_v)|nLM_L\rangle \times\sum_{M_{L_0}} {}^{2\mathcal{S}+1}f_{M_L,M_{L_0}}(\theta)\,{}^{2\mathcal{S}+1}f_{M'_L,M_{L_0}}(\theta)^* \ . \quad (54)$$

We note that the same combinations of CS scattering amplitudes ${}^{2\mathcal{S}+1}f_{M_L,M_{L_0}}(\theta)$ appear here and in the squared modulus of (39) for the dependence of the final state for electron scattering angle θ on the angular variables of the valence electron; we shall demonstrate below the connection this suggests between this intensity and that wave function. If we reexpress this result in terms of the final state in $\mathcal{E}_{nL}^{(eA)}$ that is created by electron scattering at angle θ,

$$|\mathbf{k},nL\rangle=\sum_{\mathcal{S}}(2\mathcal{S}+1)\sum_{M_L} {}^{2\mathcal{S}+1}f_{M_L,M_{L_0}}(\theta)|nLM_L;\mathcal{SM}_\mathcal{S}\rangle \ , \quad (55)$$

we regain the familiar expression for the radiation pattern in such a decay

$$I_{nL\rightarrow n_fL_f}(\beta,\theta)=\frac{2L+1}{2L_0+1}\left[\frac{k}{k_0}\right]\sum_{M_{L_f}}|\langle\mathbf{k},nL|\hat{\epsilon}\cdot\mathbf{r}_v|n_fL_fM_{L_f}\rangle|^2 \ . \quad (56)$$

There remains only to evaluate the matrix elements in (54). At this point we must therefore particularize to a specific transition. We here choose the dipole $3s\rightarrow 3p$ transitions, which are the focus of our comparisons in Sec. IV and are related via time reversal to the superelastic measurements to which we compare in Sec. V; in the sequel to this paper we shall consider transitions such as $3p\rightarrow 3p$ and $3d\rightarrow 3p$. For each spin channel, we evaluate the matrix elements of $(\hat{\epsilon}\cdot\mathbf{r}_v)$ in the natural frame, where

$$\hat{\epsilon}\cdot\mathbf{r}_v=r_v(\cos\beta\sin\theta_v\cos\phi_v+\sin\beta\sin\theta_v\sin\phi_v) \quad (57)$$

and, with $R_{nL}(r_v)$ for the radial wave function of the valence electron, we obtain

$${}^{2\mathcal{S}+1}I_{nL\rightarrow n_fL_f}(\beta,\theta)=\frac{2L+1}{2L_0+1}\left[\frac{k}{k_0}\right]\frac{1}{6}\left[\int_0^\infty R_{3p}(r_v)r_v^3R_{3s}(r_v)dr_v\right]^2 \times\left[|{}^{2\mathcal{S}+1}f_{+1,0}(\theta)|^2+|{}^{2\mathcal{S}+1}f_{-1,0}(\theta)|^2-2|{}^{2\mathcal{S}+1}f_{+1,0}(\theta)|\,|{}^{2\mathcal{S}+1}f_{-1,0}(\theta)|\cos2(\gamma-\beta)\right] . \quad (58)$$

This result confirms that the minimum and maximum of the detected intensity occur at $\beta=\gamma$ and $\gamma+\pi/2$, respectively.

Using this result in the aforementioned operational definition for the linear polarization we obtain for spin channel $\mathcal{S}$

$${}^{2\mathcal{S}+1}P_{nL}^{(\text{lin})}(\theta)=2\frac{k}{k_0}\frac{|{}^{2\mathcal{S}+1}f_{+1,0}(\theta)|\,|{}^{2\mathcal{S}+1}f_{-1,0}(\theta)|}{{}^{2\mathcal{S}+1}\sigma_{3s\rightarrow 3p}(\theta)} \ , \quad (59)$$

where the DCS for the spin channel $\mathcal{S}$ is given by Eq. (20). Regarding the similarity between Eq. (54) and the valence-electron wave function (39), we note that this is the same result we get by subtracting the maximum and the minimum values of the squared modulus of this function—and normalizing by the sum of these values [51]. (Note that the angles of the extrema of this angular probability differ from those of the intensity function by $\pi/2$; as expected from the dipole radiation pattern, the minimum and maximum occur at $\beta=\gamma+\pi/2$ and γ, re-

spectively.) This result is further explicated and illustrated in the review by Andersen, Gallagher, and Hertel [27], where care must be taken to note that their "amplitudes" a_{M_L} are not the spin-channel scattering amplitudes that appear in the boundary conditions on the wave function but rather

$$a_{M_L}=\left[\frac{k}{k_0}\right]^{1/2}\frac{^{2\mathcal{S}+1}f_{M_L,0}(\theta)}{[^{2\mathcal{S}+1}\sigma_{n_0L_0\to nL}(\theta)]^{1/2}} . \tag{60}$$

C. Experiments with both initial-state preparation and final-state analysis: Scattering of spin-polarized electrons from unpolarized atoms

In the other major class of experiments to which we compare, Hegemann *et al.* [17] determined the change in polarization of the scattering electrons due to elastic ($3s\to 3s$) and inelastic ($3s\to 3p$) e-Na collisions. These experiments provide a useful counterpart to those of the preceding subsection, since they involve both preparation of the initial state and analysis of the final state—of the electrons only. Moreover, they illustrate the application of the density operator formalism to measurements of quantities other than the detected scattering intensity. In particular, the observable of interest here is the polarization along $\hat{z}^n$ of electrons scattered at angle θ,

$$P_{n_0L_0\to nL}(\theta)=\langle\hat{\sigma}_z\rangle_{nL}=\frac{\mathrm{Tr}[\hat{\sigma}_z\hat{\rho}_{nL}]}{\mathrm{Tr}[\hat{\rho}_{nL}]} , \tag{61}$$

where $\hat{\sigma}_z$ is the projection of the Pauli spin operator along the axis of spin polarization $\hat{z}^n$ and the density operator for the final state $\hat{\rho}_{nL}$ must be constructed using the mapping (13b). Note that in the absence of continuum spin-orbit coupling, the spin projection of the projectile, and hence its polarization, can change only via exchange effects.

We first require the preparation density operator. As in the experiments of McClelland and co-workers, the polarization measurements of Hegemann *et al.* use an incident beam of electrons in a mixed state with fraction $|P_0|$ in a spin eigenstate (with $m_{s_0}=\pm\frac{1}{2}$ for $P_0=\pm|P_0|$) and the rest unpolarized. So the electron density operator is again given by Eq. (43). The atomic beam, however, is completely unpolarized, in a (mixed) state in $\mathcal{E}^{(A)}_{n_0L_0}$ represented by the operator [see Eq. (11)]

$$\hat{\rho}^{(A)}_{n_0L_0}=\frac{1}{2(2L_0+1)}\times\sum_{M_{L_0},M_{S_0}}|n_0L_0M_{L_0}M_{S_0}\rangle\langle n_0L_0M_{L_0}M_{S_0}|$$
$$=\frac{1}{2(2L_0+1)}\hat{1}_{n_0L_0} . \tag{62}$$

The resulting preparation density operator, just the direct product of these electron and atom density operators, yields especially simple matrix elements in the US basis.

To express the measured quantity—the ratio of final to initial electron spin polarization—in terms of our calculated scattering amplitudes, we evaluate the traces in the numerator and the denominator in Eq. (61) in the most convenient representation. The matrix of the preparation density operator is fully diagonal in the US representation (i.e., with respect to M_{L_0}, M_{S_0}, and m_{s_0}) and the Pauli spin operator $\hat{\sigma}_z$ is diagonal in $\mathcal{E}^{(e)}$. So evaluation of the numerator is particularly simple if we use the US basis $\{|m_{s_0},n_0L_0M_{L_0}M_{S_0}\rangle\}$ of $\mathcal{E}^{(eA)}_{n_0L_0}$. Inserting the resulting matrix elements of the final-state density operator, into the US expression for the trace,

$$\mathrm{Tr}[\hat{\sigma}_z\hat{\rho}_{nL}]=\sum_{m_s}\sum_{M_{S,M_L}}(2m_s)\langle m_s,nLM_LM_S|\hat{\rho}_{nL}|m_s,nLM_LM_S\rangle , \tag{63}$$

we obtain the eminently sensible result

$$\mathrm{Tr}[\hat{\sigma}_z\hat{\rho}_{nL}]=\frac{1}{2(2L_0+1)}\sum_{M_L,M_{L_0}}\sum_{m_s,m_{s_0}}\sum_{M_S,M_{S_0}}(\tfrac{1}{2}+m_{s_0}P_0)|f(\mathbf{k}m_s,nLM_LM_S\leftarrow\mathbf{k}_0m_{s_0},n_0L_0M_{L_0}M_{S_0})|^2 . \tag{64}$$

To introduce the singlet and the triplet amplitudes we use the Clebsch-Gordan series to convert the US amplitudes in Eq. (64) to the CS representation,

$$f(\mathbf{k}m_s,nLM_LM_S\leftarrow\mathbf{k}_0m_{s_0},n_0L_0M_{L_0}M_{S_0})=\sum_{\mathcal{S}}C(\tfrac{1}{2}\tfrac{1}{2}\mathcal{S};m_{s_0}M_{S_0})C(\tfrac{1}{2}\tfrac{1}{2}\mathcal{S};m'_{s_0}M'_{S_0})^{2\mathcal{S}+1}f_{M_L,M_{L_0}}(\theta) . \tag{65}$$

Of the six possible combinations of electron and atomic spin projections, only three are physically distinguishable, and after a little algebra we obtain

$$\mathrm{Tr}[\hat{\sigma}_z\hat{\rho}_{nL}]=\frac{P_0}{2L_0+1}\sum_{M_L,M_{L_0}}[2|^3f_{M_L,M_{L_0}}(\theta)|^2+2|^1f_{M_L,M_{L_0}}(\theta)|\,|^3f_{M_L,M_{L_0}}(\theta)|\cos\Delta_{M_L,M_{L_0}}] , \tag{66}$$

where we have introduced the triplet-singlet phase angle of Eq. (32).

Turning now to the denominator in Eq. (61), we can easily work directly in the CS representation, proceeding as in

the derivation of Eq. (45b) from Eq. (45a). We shall first write the preparation density operator in terms of projection operators onto the spin-channel eigensubspaces ${}^{2\mathcal{S}+1}\mathcal{E}^{(eA)}_{n_0L_0}$ and then take the required trace in $\mathcal{E}^{(eA)}_{nL}$,

$$\mathrm{Tr}[\hat{\rho}_{nL}]=\sum_{M_L,\mathcal{S},\mathcal{M}_\mathcal{S}}\langle nLM_L;\mathcal{S}\mathcal{M}_\mathcal{S}|\hat{\rho}_{nL}|nLM_L;\mathcal{S}\mathcal{M}_\mathcal{S}\rangle\ . \tag{67}$$

Evaluating the necessary sums is especially simple because of the diagonal character of the CS matrix of $\hat{\rho}^{(\mathrm{prep})}_{n_0L_0}$, and we obtain

$$\mathrm{Tr}[\hat{\rho}_{nL}]=\frac{1}{2(2L_0+1)}\sum_{M_L,M_{L_0}}\sum_{\mathcal{S},\mathcal{M}_\mathcal{S}}|{}^{2\mathcal{S}+1}f_{M_L,M_{L_0}}(\theta)|^2\left\{\sum_{m_{s_0}}(\tfrac{1}{2}+m_{s_0}P_0)[C(\tfrac{1}{2}\tfrac{1}{2}\mathcal{S};m_{s_0}M_{S_0})]^2\right\}\ . \tag{68}$$

Note that the quantity in curly brackets also appeared in Eq. (48) for the detected scattering intensity measured by McClelland and co-workers. But unlike that result, the present final-state polarization combines an average over initial and sum over final magnetic sublevels with a sum over total spin quantum numbers that accommodates both possible final atomic spin states. Both are required by the experimental design of Hegemann *et al.*, which does not prepare or analyze the atomic states with respect to their orbital or spin angular momentum. Finally, we note that by further evaluating the sums over $\mathcal{S}$, $\mathcal{M}_\mathcal{S}$, and m_{s_0}, we can reduce Eq. (68) to the spin-averaged DCS of Eq. (19), as

$$P_{n_0L_0\to nL}(\theta)=\frac{2P_0}{2L_0+1}\left[\frac{k}{k_0}\right]\frac{1}{\bar{\sigma}_{n_0L_0\to nL}}\sum_{M_L,M_{L_0}}\left[|{}^3f_{M_L,M_{L_0}}(\theta)|^2+|{}^1f_{M_L,M_{L_0}}(\theta)|\,|{}^3f_{M_L,M_{L_0}}(\theta)|\cos\Delta_{M_L,M_{L_0}}\right]\ . \tag{69}$$

This analysis yields the ratio of the final to initial electron-spin polarization, the measured quantity in these experiments. Useful relationships for elastic scattering between this quantity and the triplet-singlet ratio $r(\theta)$ and the phase angle $\Delta_{0,0}$ and for $3s\to3p$ scattering between these quantities and the spin-channel angular momentum transfers have been presented by Andersen and Bartschat [51,52].

IV. A BIRD'S-EYE VIEW OF ELASTIC AND INELASTIC OA PARAMETERS

Several investigators have reported low-energy e-Na scattering experiments of the kinds described in Sec. III and we shall compare our result to their data in Sec. V. But these measurements encompass a necessarily limited range of scattering angles and, more to the point, very few energies: indeed, almost all are near 4.0 eV, an energy that is rich in structure because of the proximity of a large number of target thresholds but that for this very reason is anomalous. One advantage of the R-matrix method used in our study is the comparative ease and modest computational demands of solving the continuum Schrödinger equation at a large number of energies, once a considerable initial investment has been made at a single energy. This feature enables us to contextualize the comparisons in Sec. V by here surveying the behavior of elastic and inelastic OA parameters over the whole range of scattering angle from 0° to 180° and energy from threshold to 8.6 eV. The results, presented in this section as three-dimensional graphs, both clarify trends evident in the single-energy "snapshots" in Sec. V and suggest energies where further measurements may provide fruitful tests of experiments and contributions to our growing understanding of this paradigmatic electron-atom collision system.

A. Elastic scattering

At energies below a few eV, the spin-averaged elastic DCS $\bar{\sigma}_{3s\to3s}(\theta)$ is dominated by a pronounced structure near the $3p$ threshold at 2.1 eV, as illustrated in Fig. 13 of Ref. [1]. In Fig. 3 we here expand this view of the elastic DCS to encompass energies up to 8.6 eV, plotting its logarithm so as to more clearly show the variation over the range of the figure. This perspective clarifies the characteristic structural change from comparable forward and

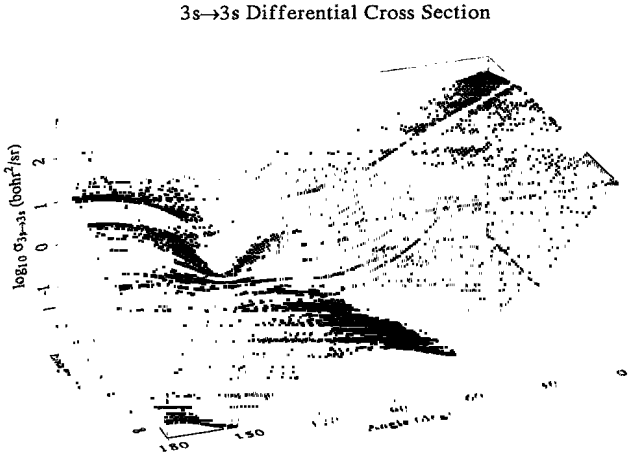

FIG. 3. Logarithm of the spin-averaged elastic differential cross section $\bar{\sigma}_{3s\to3s}(\theta)$.

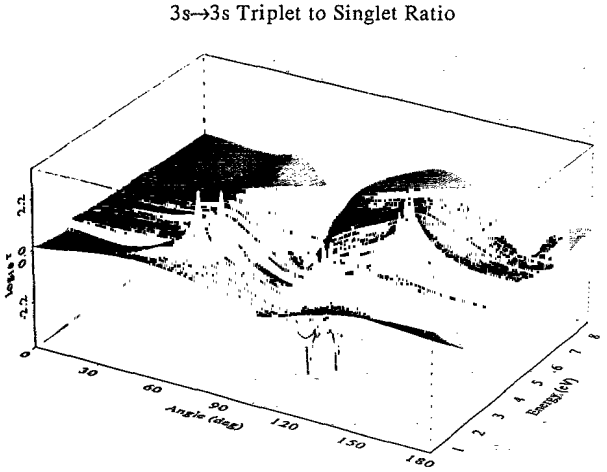

FIG. 4. Logarithm of the M_L-averaged elastic triplet-singlet ratio $r_{3s\to 3s}(\theta)$.

backward scattering at the low-energy end of this range to pronounced forward scattering at the high-energy end.

To explore the contributions to elastic scattering from the triplet and the singlet spin channels we show in Fig. 4 the logarithm of the triplet-to-singlet ratio defined in Eq. (29). Since the $3s\to 3s$ transition admits only $M_L=0$, the quantity here shown is

$$\log_{10} r(\theta)=\log_{10}\left[\frac{{}^3\sigma_{3s\to 3s}(\theta)}{{}^1\sigma_{3s\to 3s}(\theta)}\right] . \quad \text{(70)}$$

[For clarity in this and subsequent three-dimensional (3D) figures, we have set the orientation differently than in Fig. 3.] This overview reveals several sharp "peaks" and "valleys" that are caused by (near) zeros in the singlet and the triplet DCSs, respectively. Such sharp structures are particularly likely to appear in the $3s\to 3s$ triplet-to-singlet ratio since the spin-channel DCSs involve only the $M_L=M_{L_0}=0$ magnetic substate. (The structures around $\theta=120°$ in this figure appear more jagged than they really are due to the inability of the plotting program to smoothly depict a sharp ridge that shifts in both angle and energy.) The enhancement of scattering in the singlet channel revealed by the valley between 90° and 60° above 4 eV arises from a minimum in the triplet cross section.

The final elastic OA parameter is the triplet-singlet phase angle $\Delta_{0,0}(\theta)$, the cosine of which, shown in Fig. 5, manifests a far more complicated variation with angle and energy than the spin-averaged DCS and triplet-singlet ratio, which together determine the *magnitudes* of the spin-channel scattering amplitudes. Of particular note is the variation of this quantity with scattering angle, which over the whole energy range is far richer than one might infer from the single energy (4.1 eV) at which it has been studied experimentally. Rapid changes in this phase angle are correlated with near zeros in the singlet or the triplet DCS, the peaks and valleys in Fig. 4.

B. Inelastic scattering

For the $3s\to 3p$ transition, more and more varied parameters are amenable to measurement in superelastic and coincidence experiments as described in Sec. III. The inelastic spin-averaged DCS in Fig. 6 shows a variation with angle and energy very much like that of its elastic counterpart in Fig. 3: very little angular variation at low energies and an increased propensity for forward scattering with increasing energy. The rapid increase with energy in the forward peak of this DCS contrasts markedly with the near independence of energy of the elastic DCS in the forward direction.

Like all the OA parameters surveyed in this section, $\bar{\sigma}_{3s\to 3p}(\theta)$ exhibits considerable structure in the energy range from 4.0 to 4.6 eV, where thresholds reside for the 5s, 4d, 4f, 5p, 6s, 5d, and 6p target states (see Table I of Ref. [1]). (This region is marked by a rich panoply of narrow structures; the energy grid in the present calcula-

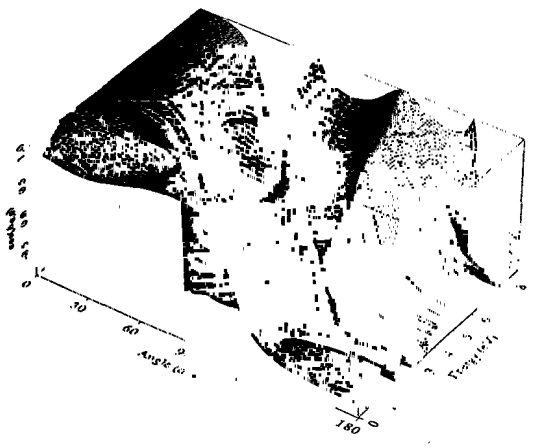

FIG. 5. Cosine of the elastic triplet-singlet phase angle $\Delta_{0,0}(\theta)$.

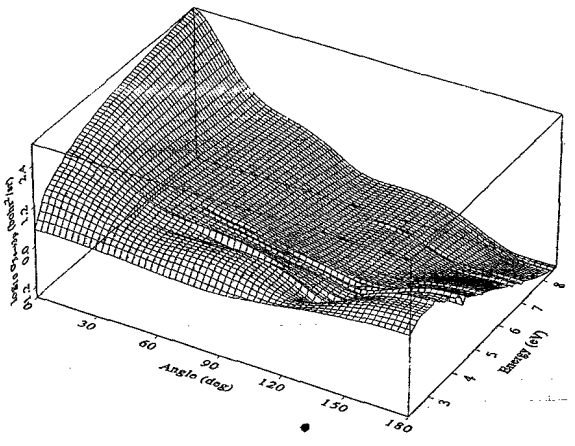

FIG. 6. Logarithm of the $3s\to 3p$ spin-averaged differential cross section $\bar{\sigma}_{3s\to 3p}(\theta)$.

tions indicates characteristic behavior in this region, but is not sufficiently dense to show all of its structures.)

The $3s \rightarrow 3p$ triplet-singlet ratio whose logarithm is shown in Fig. 7 exhibits strong singlet dominance near the $3p$ threshold at 2.1 eV, another consequence of the near-threshold structure in the singlet channel. Note that the sharp structures of the elastic ratio in Fig. 4 are missing. In this case, the spin-channel DCS are the sums of the squares of the two nonzero $s \rightarrow p$ amplitudes, which sums wash out this structure.

We note, however, that the dominance of triplet scattering at higher energies for scattering near 60° and 120° will enhance the spin polarization of inelastically scattered electrons at these angles, a feature of possible future usefulness to experiments such as those discussed in Sec. V. The small-angle behavior of this quantity shows that except near the $3p$ threshold, forward scattering is almost equally probable into the triplet and the singlet channels. This result reflects the influence at these angles of elements of the transition matrix that correspond to large orbital angular momenta; because of the strong centrifugal barriers that control the corresponding elements of the scattering function, these T-matrix elements are quite insensitive to exchange, as illustrated in Fig. 1 of Ref. [1].

The relative phase between the triplet and the singlet scattering amplitudes is graphed for the $+1$ magnetic sublevel in Fig. 8. This angle, which varies from $-180°$ to $+180°$, is especially interesting in the forward direction, where the threshold structure at 2.1 eV sends it sharply negative near this energy. As energy increases away from this threshold, however, the triplet-singlet phase angle settles down essentially to zero. The abrupt change in $\Delta_{+1,0}(\theta)$ at high energy and large scattering angle is caused by a minimum in the singlet cross section.

The other relative phase angles for $3s \rightarrow 3p$ scattering are the singlet and the triplet alignment angles defined in Eq. (38). These angles, which reveal the proximity of the symmetry axis of the final-state wave function of the valence electron to the incident electron direction (the axis $\hat{x}^n$ of the natural frame), are defined to lie between $-90°$ and $+90°$ and so can change abruptly by 180° when the angle of the $3p$-state symmetry axis exceeds 90°, as happens at several places in Fig. 9. Near the $3p$ threshold, for example, ${}^3\gamma(\theta)$ changes by a total of 360° as the

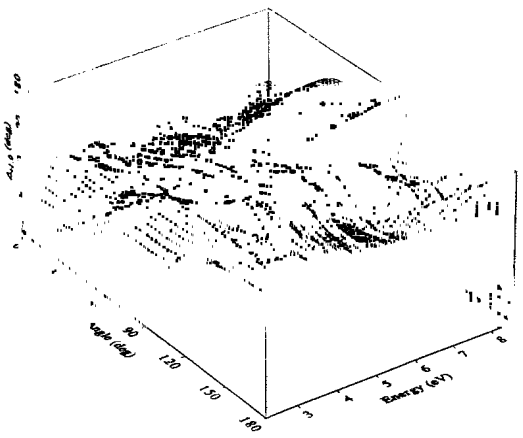

FIG. 8. $3s \rightarrow 3p$ triplet-singlet phase angle $\Delta_{+1,0}(\theta)$.

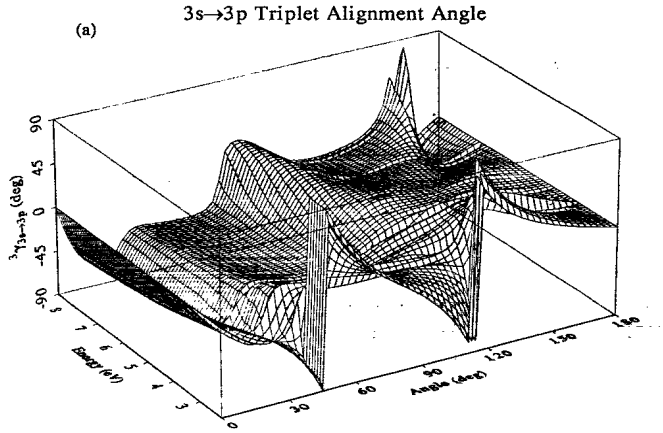

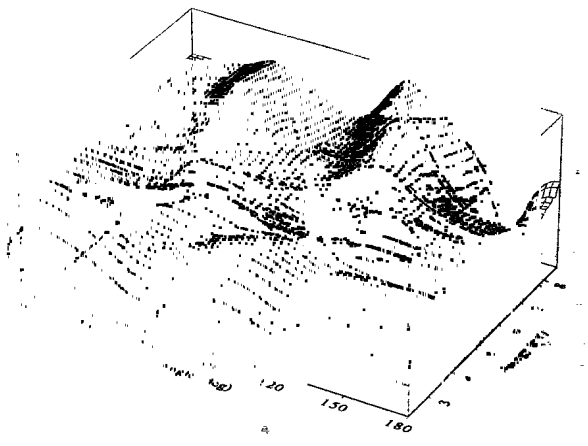

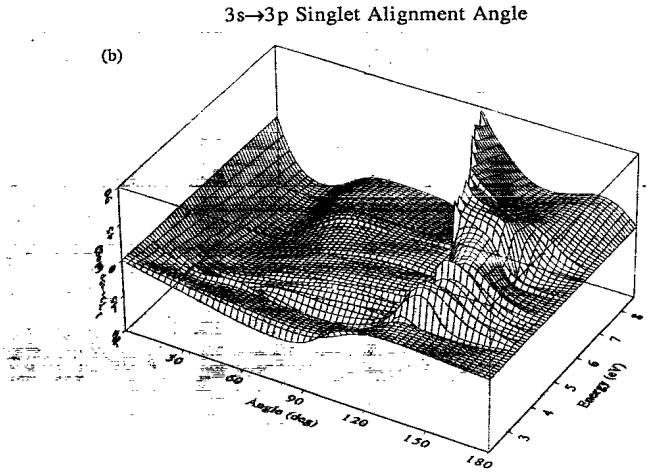

FIG. 7. Logarithm of the M_L-averaged $3s \rightarrow 3p$ triplet-singlet ratio $r_{3s \rightarrow 3p}(\theta)$.

FIG. 9. $3s \rightarrow 3p$ (a) triplet and (b) singlet alignment angles ${}^3\gamma_{3s \rightarrow 3p}(\theta)$.

scattering angle varies from 0° to 180°. Both alignment angles are zero for $\theta=0°$ and $\theta=180°$. The final-state wave function can have no component in the $\hat{z}^n$ direction since ${}^{2S+1}f_{0,0}(\theta)=0$. For straight-line collisions, then, there is no distinction between $\hat{z}^n$ and $\hat{y}^n$ directions, so the symmetry axis of the charge cloud must lie in the $\hat{x}^n$ direction. For forward scattering, the alignment angles confirm the result predicted by the first-Born approximation, that the final-state wave function is oriented along the momentum-transfer vector $\mathbf{k}-\mathbf{k}_0$.

Rather more illuminating is the final $3s\rightarrow 3p$ OA parameter, the angular-momentum transfer. By exhibiting the average angular momentum transferred to the atom normal to the scattering plane, ${}^{2S+1}L^{(\perp)}_{3s\rightarrow 3p}(\theta)$ reveals the relative importance of the $M_L=\pm 1$ magnetic sublevels in the final $3p$ atomic state created by scattering at a particular angle θ. In Fig. 10 we find considerable similarities between the angular-momentum transfers in the two spin channels. Both are zero for $\theta=0°$ and 180°, as they must be since angular momentum cannot be transferred in forward or backward collisions. Both angular-momentum transfers show that in the forward direction, scattering into the $M_L=+1$ substate dominates; this effect is most prominent in ${}^3L^{(\perp)}(\theta)$. Above about 90° (for the triplet channel) and 120° (for the singlet channel), both quantities exhibit a distinct minimum.

The overview provided by all the three-dimensional graphs for the $3s\rightarrow 3p$ transition reveals several interesting interconnections between the seven OA parameters. For example, as $\theta\rightarrow 0$, the triplet-singlet ratio r approaches unity, and the angular-momentum transfers ${}^3L^{(\perp)}_{3s\rightarrow 3p}(\theta)$ and the three phase angles go to zero. This means that in the forward direction, all four amplitudes ${}^{2S+1}f_{M_L,0}(\theta)$ for $2S+1=1$ and 3 and for $M_L=\pm 1$, are nearly equal; i.e., for this transition forward scattering does not depend strongly on magnetic or spin-projection quantum numbers.

Several of these figures reveal sharp structures arising from abrupt changes in one of the OA parameters. These structures tend to be associated with minima in the spin-channel and/or spin-averaged DCSs. For example, the minimum in $\bar{\sigma}_{3s\rightarrow 3p}(\theta)$ at 120° triggers rapid changes in other OA parameters. The minimum in the triplet DCS at energies above 5.0 eV at angles between 155° and 160° manifests itself at these energies and scattering angles as a pronounced minimum in the triplet-singlet ratio and abrupt changes in the triplet-singlet phase angle and the triplet alignment angle. Just as these overviews may guide future measurements towards particularly interesting regions of energy and angle, so may such interconnections guide them away from energy and angle regions where the scattered electron count rate is likely to be uncomfortably small.

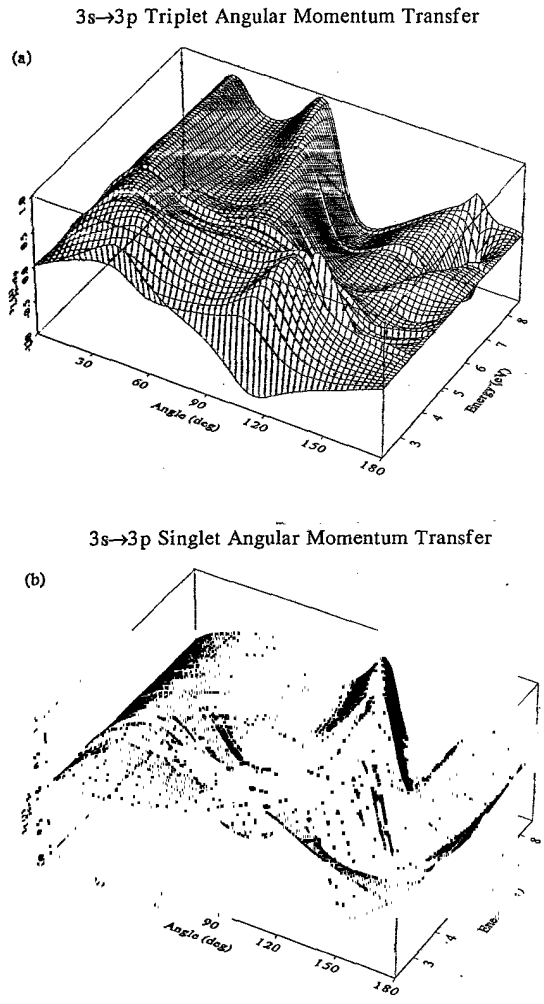

FIG. 10. $3s\rightarrow 3p$ (a) triplet and (b) singlet angular-momentum transfer perpendicular to the scattering plane ${}^3L_\perp(\theta)$.

V. COMPARISON OF THEORETICAL AND EXPERIMENTAL ORIENTATION AND ALIGNMENT PARAMETERS

We now turn to several measurements that together approach the asymptote of complete scattering experiments for low-energy elastic ($3s\rightarrow 3s$) and inelastic ($3s\rightarrow 3p$) e-Na collisions. The OA parameters measured in these experiments provide a more detailed probe of the dynamics than do the conventional DCSs. For example, for low-energy inelastic transitions involving low-Z atoms such as Na, these parameters yield insight into exchange effects, which manifest themselves in experiments in which the initial state is prepared so the electrons (and possibly the atoms) are spin polarized. The particular parameters one can measure in such experiments depend on whether one analyzes the final state.

As described in Sec. II of the first paper of this series [1], the R-matrix formulation we use to calculate the CS scattering amplitudes follows from two key expansions of the e-Na wave function: in bound stationary states of the target and in angular functions of the projectile (spherical harmonics); in practice these expansions must be truncated at some total number of target states and partial waves. In Sec. IV of that paper we demonstrated the convergence integral and differential elastic and inelastic cross sections with respect to both of these expansions. But the upper limits of the eigenfunction expansions

thereby determined do not necessarily guarantee convergence of the more sensitive OA parameters to be shown in the present paper and its sequel. Some of these parameters depend on products of spin amplitudes for different magnetic sublevels, quantities not sampled even by the DCS. Moreover the conventional DCSs and ICSs involve averages over initial and sums over final atomic magnetic sublevels, which decreases their sensitivity to high-lying target states and large-order partial waves.

A. Elastic scattering

For elastic scattering, the three parameters (33) fully characterize the collision. For the first of these—the spin-averaged DCS $\bar{\sigma}_{3s\to 3s}(\theta)$—we have already discussed convergence properties and compared them to experiment in Figs. 11 and 13–18 of Ref. [1]. For the second, we choose the exchange asymmetry rather than the triplet-singlet ratio, because the former is less sensitive to normalization factors. In Fig. 11, we show both convergence studies and a comparison to measured results at 1.0, 1.6, and 4.1 eV, the only energies at which these data have been measured.

In the convergence studies to follow, we have calculated scattering parameters using a four-state close-coupling model (4CC), which includes the 3*s*, 3*p*, 4*s*, and 3*d* target states, a 7CC model, which adds to these four the 4*p*, 4*d*, and 4*f* states, and a 10CC model, which further adds the 5*s*, 5*p*, and 5*d* states. We have also performed two 11CC calculations; the 11CC(6*s*), which also includes the 6*s* state, and the 11CC(6*p*), which includes instead the 6*p* state. To illustrate the quality of the convergence of the exchange asymmetry, we compare our 4CC and 10CC results with those of Bray and McCarthy [39]. At the higher energy we also show the 7CC and 11CC(6*s*) and 11CC(6*p*) results. Clearly, the 10CC results are well converged over the range of scattering angles; the most pronounced differences from the 4CC results occur at the peaks near 115° at 1.0 eV, 110° at 1.6 eV, and above 90° at 4.1 eV. The 11CC results at the higher energy illustrate the degree of convergence even in this sensitive angular region.

A unique feature of the present calculations concerns the treatment of the neonlike core of the Na target. As discussed in Sec. III B of Ref. [1], our description of the electron-Na interaction includes, in addition to the usual one-electron terms that represent the polarization of the core due to the valence and projectile electrons, a dielectronic term that allows for the interaction of the dipole moments resulting from these two one-electron polarization effects. To explore the importance of this term for $A_0^{(ex)}(\theta)$ we here show results [denoted 10CC(ND)] from calculations in which we *omitted* the dielectronic polarization term. Comparisons to the 10CC values show sensitivity to this effect to be greatest near the aforementioned peaks. Somewhat surprisingly, at 1.0 eV the 10CC results agree better with those from 4CC calculations than from the 10CC(ND) study; this suggests that at low energies including dielectronic polarization is more important than including high-lying target states such as the six additional states of the 10CC calculations.

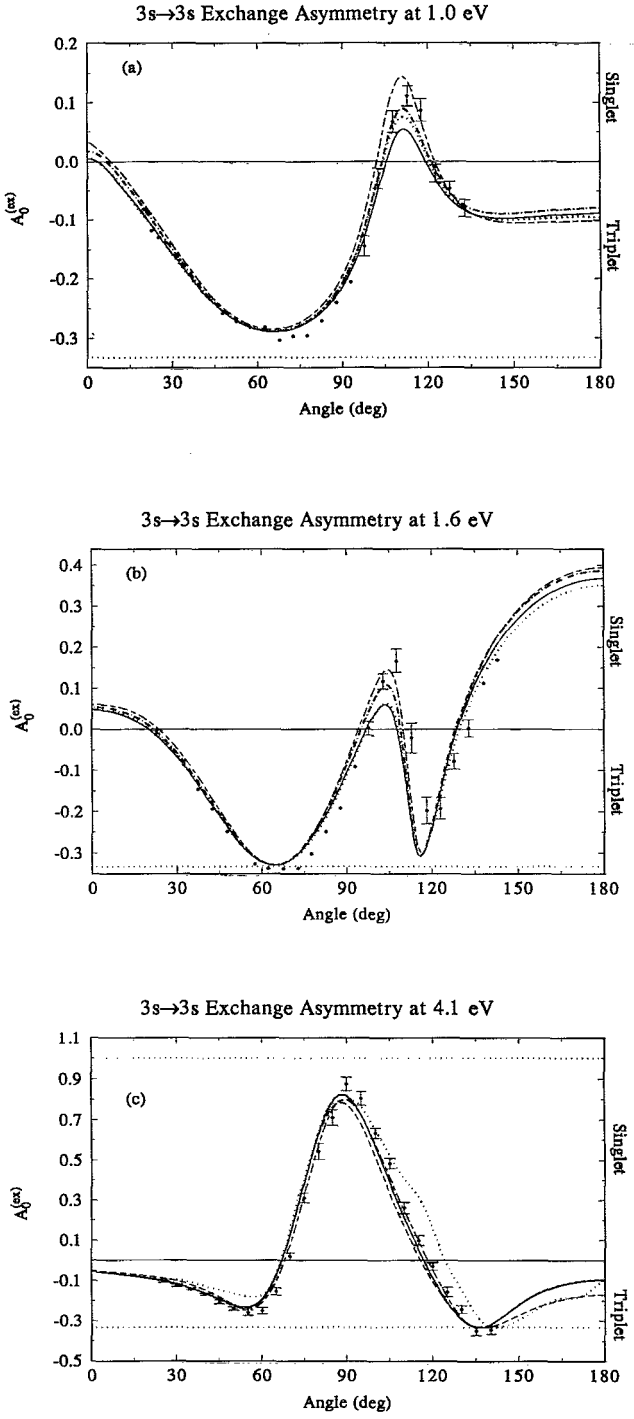

FIG. 11. Comparison of the elastic exchange asymmetry $A_0^{(ex)}(\theta)$ at (a) 1.0 eV, (b) 1.6 eV, and (c) 4.1 eV as measured by Lorentz *et al.* [15] (solid points with error bars) and as calculated by Bray and McCarthy [39] (long-dash–short-dashed curve). Our theoretical curves are from the following calculations (see text for acronyms): 11CC(6*p*) (short-dashed curve), 11C(6*s*) (long-dashed curve), 10CC(ND) (dot-dashed curve), 10CC (solid), 7CC (medium-dashed curve), and 4CC (dotted curve). The dotted horizontal lines indicate maximum and minimum allowed values of this quantity. Note that the 7CC, 11CC(6*s*), and 11CC(6*p*) results appear only in (c). Some of the curves in this figure overlap throughout the angular range shown; although indistinguishable, these results do confirm convergence.

At these energies we can compare our results to those from a quite-differently formulated theoretical study by Bray and McCarthy [39], which included 15 target states but not dielectronic polarization. At the lowest energies in Figs. 11, the difference between the 15CC(ND) results of Bray and McCarthy and our 10CC(ND) values is as large or larger than that between our 10CC and 4CC results—a finding with the surprising implication that adding five additional states to a calculation that already includes ten could change the elastic asymmetry by as much as adding six additional states to a 4CC calculation. At 4.1 eV, agreement between our converged elastic exchange asymmetries and those calculated by Bray and McCarthy using a full optical potential is better, suggesting that at this energy higher-lying target states do not significantly influence this parameter.

A comparison to measured elastic exchange asymmetries at 1.0 and 1.6 eV [15] and 4.1 eV [13] essentially confirms the observations of McClelland and co-workers of a significant dependence of $A_0^{(\mathrm{ex})}(\theta)$ on scattering angle and of the dominance of triplet scattering at 1.0 and 4.1 eV (below 120°) but not at 4.1 eV, where singlet scattering predominates from about 70°–120°. Agreement between theoretical and experimental elastic asymmetries is excellent, except in the vicinity of the peak. These comparisons (and those to the theoretical results of Bray and McCarthy) essentially benchmark the wide range of results shown in the 3D graphs of Sec. IV. These graphs make clearer the context of the trends in Fig. 11 and suggest other energies and angular regions where measurement of this parameter may prove fruitful.

Elastic scattering amplitudes

In a remarkable illustration of the power of the experiments discussion in Sec. III to probe collision dynamics, McClelland *et al.* [13] combined their measured values of the elastic triplet-singlet ratio $r(\theta)$, which is equivalent to the elastic exchange asymmetry through Eq. (31), and the spin-averaged elastic DCS as measured by Gehenn and Reichert [53] to determine the magnitudes of the singlet and triplet $3s \rightarrow 3s$ amplitudes. In Fig. 12 we compare their magnitudes to our converged 10CC amplitudes, obtaining good agreement over the angular range of the experiment from 30° to 130°.

Unfortunately, a question has hovered over this determination because the two measurements were performed at slightly different energies and the widths are quite broad: 4.1±0.25 eV for McClelland *et al.* [13] and 4.0±0.05 eV for Gehenn and Reichert [53]. Because of our detailed knowledge of the energy variation of both parameters we are in a position to resolve this question. We have already compared our 4.0-eV elastic DCSs to those of Gehenn and Reichert in Fig. 18(b) of Ref. [1] and found excellent agreement throughout the angular range from about 25° to 150°. We have calculated a second set of amplitudes from 10CC triplet-singlet ratios at 4.1 eV and elastic DCSs at 4.0 eV. As seen in Fig. 12, the effect of the slight energy mismatch in the two experiments is entirely negligible—an unsurprising result that nonetheless seems important in light of the seminal character of

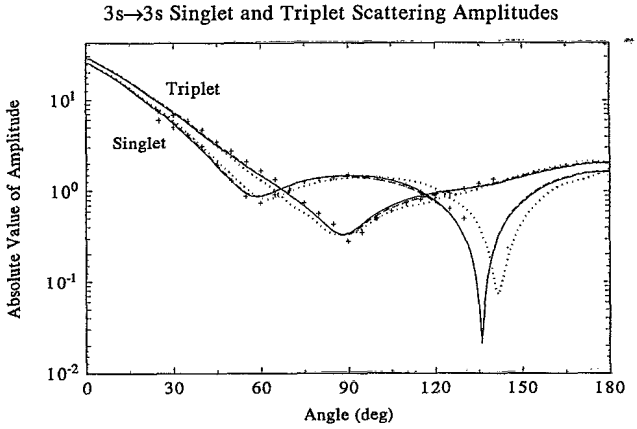

FIG. 12. Absolute values of the elastic scattering amplitudes for the singlet $|^1f_{3s\rightarrow 3s}(\theta)|$ and triplet $|^3f_{3s\rightarrow 3s}(\theta)|$ spin channels. Experimental points (pluses) were generated by combining the triplet-to-singlet ratio of McClelland, Kelley, and Celotta [11], which were measured at 4.1 eV, with the differential cross sections of Gehenn and Reichert, which were measured at 4.0 eV [53]. The theoretical data are from 10CC (solid curve) and 4CC (dotted curve) calculations at 4.1 eV. Also shown is a simulation of the energy mismatch (medium-dashed curve) constructed by combining the 10CC triplet-to-singlet ratio at 4.1 eV with the 10CC DCS at 4.0 eV.

the determination by McClelland and co-workers [15]. Finally, we note that a poorer representation of the target (the 4CC study) affects the amplitudes primarily at larger angles.

Continuing their analysis of the elastic amplitudes, McClelland and co-workers determined the cosine of the triplet-singlet phase angle $\Delta_{0,0}(\theta)$ of Eq. (32) by combining their 4.1-eV values for $r(\theta)$ with data from measurements by Hegemann *et al.* [17] of the final-state electron

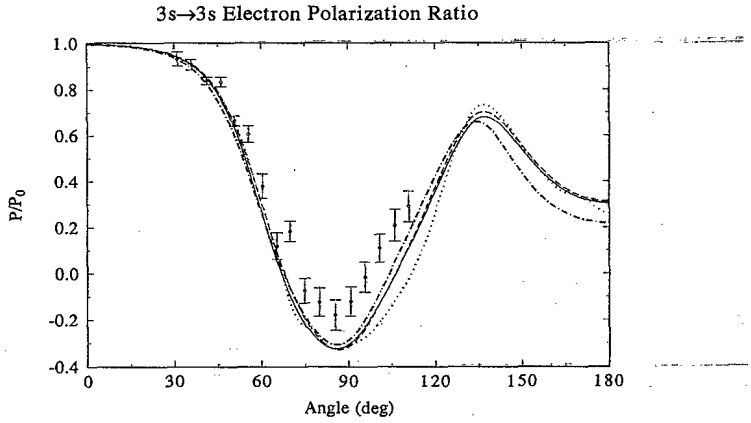

FIG. 13. Comparison of theoretical elastic electron polarization ratio $P_{3s\rightarrow 3p}(\theta)$ at 4.0 eV to experimental data of Hegemann *et al.* [17] (solid circles with error bars). The theoretical curves are 10CC at 4.0 eV (solid curve), 7CC at 4.0 eV (medium-dashed curve), 4CC at 4.0 eV (dotted curve), and finally we include the 10CC calculations at 4.1 eV (dot-dashed curve) because this experimental data has (here and elsewhere) been compared to calculations at 4.1 eV.

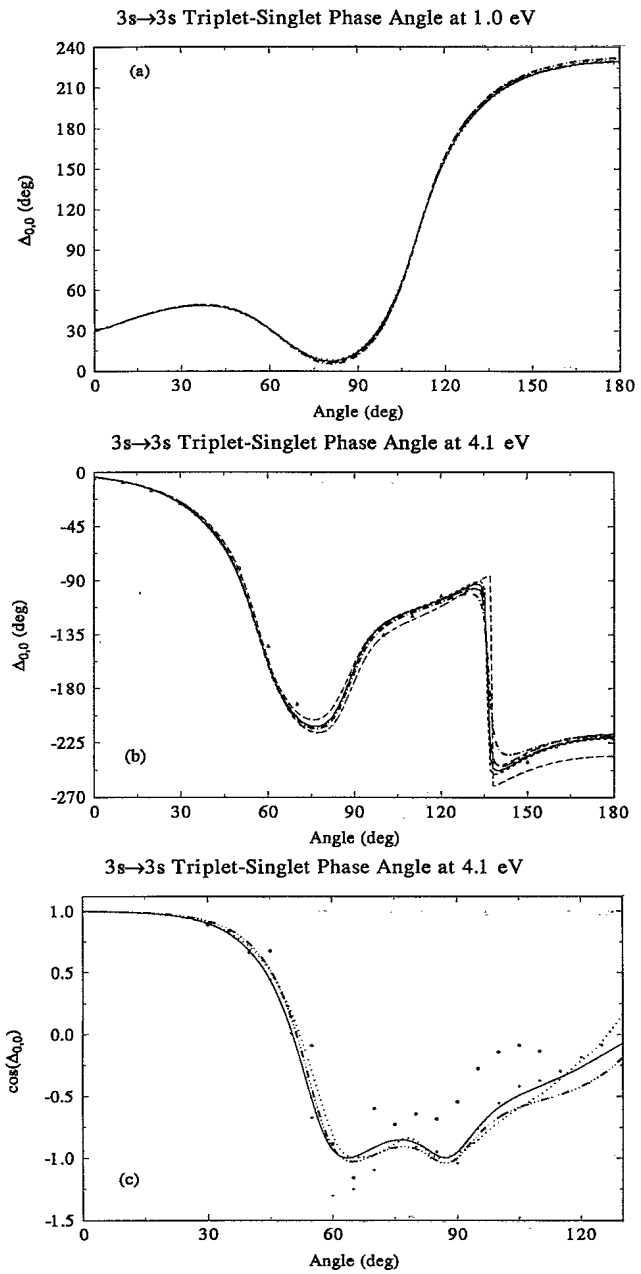

FIG. 14. (a) Convergence of the triplet-singlet phase angle for elastic scattering $\Delta_{0,0}(\theta)$ at 1.0 eV. (b) Convergence of the triplet-singlet phase angle at 4.1 eV. (c) Measured and calculated values of the cosine of the elastic triplet-singlet phase angle $\cos[\Delta_{0,0}(\theta)]$. The theoretical curves are from Bray (long-dash–short-dashed curve) and present 10CC(ND) (dot-dashed curve), 11CC($6p$) (short-dashed curve), 11CC($6s$) (long-dashed curve), 10CC (solid curve), 7CC (medium-dashed curve), and 4CC (dotted curve) calculations. Experimental points (solid circles) in (c) were generated by combining the triplet-to-singlet ratio of McClelland *et al.* [13], which were measured at 4.1 eV, with the polarization ratio of Hegemann *et al.* [17] (solid circles). (Note that the algebraic relation that gives $\cos[\Delta_{0,0}(\theta)]$ from the exchange asymmetry and the electron polarization ratio does not restrict the result to the range $[-1,+1]$ (see the text).) Also shown in (c) is a simulation of the energy mismatch (triplet-dot–dashed curve) constructed by combining the 10CC triplet-to-singlet ratio at 4.1 eV with the 10CC polarization ratio at 4.0 eV.

polarization (69). While the exchange asymmetry, through its relationship to the triplet-to-singlet ratio, describes the relative magnitudes of the singlet and triplet scattering amplitudes, the phase angle $\Delta_{M_L,M_{L_0}}(\theta)$ defined in Eq. (32) describes their relative phases. An energy mismatch again clouded this determination, since the latter measurements were performed at 4.0 eV.

The comparison in Fig. 13 of results from 4CC, 7CC, and 10CC calculations at 4.0 eV demonstrates that the latter is well converged even at large angles. A comparison to the experimental results of Hegemann *et al.* shows excellent agreement at small angles but an experimental minimum at the polarization ratio at 90° that is shallower than in our results. Finally, comparing 10CC results at 4.0 and 4.1 eV reveals that except at very large scattering angles, this quantity is insensitive to small changes in the scattering energy. For the angular range of the measured data, then, this energy mismatch is insignificant.

We see in Fig. 14(c) that the effect of the slight energy mismatch inherent in the determination from experiment of the cosine of the relative phase angle between the triplet and the singlet amplitudes is somewhat more serious than was the case for their magnitudes in Fig. 12, especially for scattering angles greater than 60°. But this mismatch is not, apparently, solely responsible for the differences between the experimentally and theoretically determined values of $\Delta_{0,0}(\theta)$ in this angular range. To further diagnose this difference, we have evaluated this quantity using the 4.1 eV values for $r(\theta)$ measured by McClelland and co-workers and the theoretical electron-spin polarization ratio from Fig. 13; the results shown in Fig. 14(c) agree very well with the purely theoretical phase angles, suggesting that the polarization ratio and not the triplet-singlet ratio is responsible for the pronounced differences between the theoretical and the experimentally determined values of $\cos\Delta_{0,0}(\theta)$.

The triplet-singlet phase angle itself, which is shown at 1.0 eV in Fig. 14(a) and at 4.1 eV in Fig. 14(b), is extremely well converged with just four states at 1.0 eV and with 10 states at 4.1 eV, where the variation with scattering angle is representative of the whole energy range shown in the 3D figures in Sec. IV. At both energies, our results concur very well with those of Bray and manifest little sensitivity to dielectronic polarization effects. It is somewhat surprising, considering the nature of $\Delta_{0,0}(\theta)$, that this quantity is less sensitive to effects due to dielectronic polarization and high-lying atomic states than is the elastic exchange asymmetry $A_0^{(ex)}(\theta)$ [54].

B. Inelastic scattering

Of the seven parameters in Eq. (42) required to fully characterize the $3s\rightarrow 3p$ transition, four have been measured, three of them at 4.1 eV only. We showed the spin-averaged DCS for this transition and compared to experimental data in Figs. 19 and 20 of Ref. [1].

The overall importance of triplet versus singlet scattering at 4.1 eV is evident from the triplet-singlet ratio in Fig. 15, which shows the scattering to be predominantly singlet in character for most of the angular range. Com-

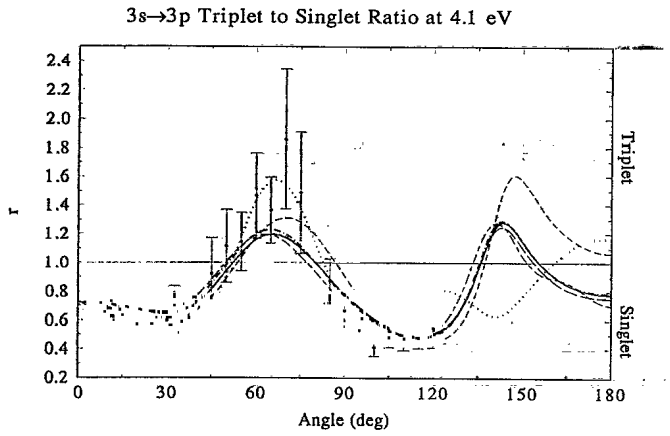

FIG. 15. Inelastic $3s \rightarrow 3p$ triplet-to-singlet ratio at 4.1 eV as measured by McClelland, Kelley, and Celotta [11] (solid circles), calculated by Bray [40] (long-dash–short-dashed curve), and generated in the present study from the following calculations described in the text: 10CC(ND) (dot-dashed curve), 11CC($6p$) (short-dashed curve), 11CC($6s$) (long-dashed curve), 10CC (solid curve), 7CC (medium-dashed curve), and 4CC (dotted curve).

paring the 4CC, 7CC, and 10CC results reveals the importance of the high-lying $n=4$ and 5 target states to an accurate calculation of the inelastic triplet-singlet ratio. Further comparisons to the two 11CC calculations and Bray's results show that these still higher-lying states are less significant and the 10CC values are converged. Finally, by comparing the latter to 10CC(ND) results and to Bray's values we find that the effects of dielectronic polarization are comparable to those of including the $n=6$ states. Agreement with the experimental data of McClelland, Kelley, and Celotta [11] is gratifying, except near the peak at 65°.

1. *Angular-momentum transfer*

Other than the triplet-singlet ratio, the most extensively measured OA parameter for this excitation is the angular-momentum transfer Eq. (35). The spin average of this parameter at 4.1 eV shows the propensity of scattering at all but the largest angles for leaving the atom in an $M_L=+1$ magnetic sublevel. Agreement with the measured data of McClelland, Kelley, and Celotta [11] is excellent at angles below 90°, as is concurrence with the 15CC(ND) theoretical values of Bray at all angles. The contributions to the angular-momentum transfer from the individual spin channels are shown in Figs. 16(a) and 16(b). In the triplet channel, our 4CC and 7CC theoretical values show that the pronounced discrepancy at angles greater than 40° noted by McClelland, Kelley, and Celotta between their experimental results and values from an earlier 4CC calculations of Moores and Norcross [43] arises from the incomplete $n=4$ target manifold in the latter. Further comparisons to 10CC results show the 7CC values to be well converged at all angles. The discrepancy between theoretical and experimental values above 90° remains unresolved.

The situation in the singlet channel is less satisfactory. The theoretical calculations converge quite slowly with increasing numbers of target states (even at small angles) and the disagreement between theory and experiment is more substantial than in the triplet channel. Comparisons to our 11CC results and to those of Bray show that the 10CC values are well converged and that the coincidence of the experimental and 7CC values is clearly an accident, at least for scattering angles less than 110°. We note further that our converged results do not agree with Bray's values near the peak at 40°. These differences probably reflect two physical distinctions between our work and his. First, he includes polarization effects ("coupling to the continuum") via an optical potential, in contrast to our semiempirical model potential. Second, he does not take into account dielectronic polarization—admittedly a minor effect at these energies.

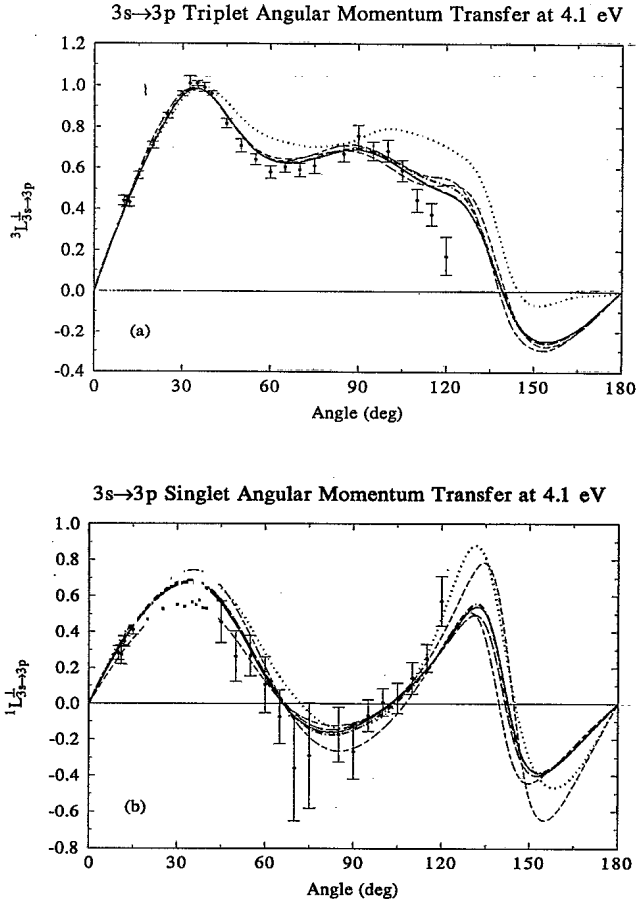

FIG. 16. (a) Triplet and (b) singlet angular-momentum transfer $L^{(1)}_{3s\rightarrow 3p}(\theta)$ at 4.1 eV as measured by McClelland, Kelley, and Celotta [11] (solid circles), calculated by Bray [40] (long-dash–short-dashed curve), and calculated in the present study using the following models: 10CC(ND) (dot-dashed curve), 11CC($6p$) (short-dashed curve), 11CC($6s$) (long-dashed curve), 10CC (solid curve), 7CC (medium-dashed curve), and 4CC (dotted curve).

2. *Inelastic scattering amplitudes*

Measurements of the four parameters $\bar{\sigma}_{3s\to 3p}(\theta)$, $r_{3s\to 3p}(\theta)$, ${}^{1}L^{(\perp)}_{3s\to 3p}(\theta)$, and ${}^{3}L^{(\perp)}_{3s\to 3p}(\theta)$ suffice to extract the magnitudes of the four scattering amplitudes ${}^{2S+1}f_{\pm 1,0}(\theta)$. The DCS has been measured at 2.6, 3.1, and 3.6 eV [55,56] and at 3.7 eV [53]. But measurements of the remaining three parameters have been reported only at 4.1 eV. This energy mismatch is too large to allow combining these data to construct the magnitudes of the singlet and triplet amplitudes. We can, however, perform this construction by combining theoretical DCSs at 4.1 eV with the measured parameters of McClelland, Kelley, and Celotta [11]. The results appear in Fig. 17 along with selected other constructs.

In the forward direction, scattering into the $M_L=+1$ substate is dominant in both spin channels. The purely theoretical triplet amplitudes agree very well with those constructed from experimental values, except at very large angles and near the deep minimum at 40°. In the singlet channel, agreement is less satisfying, as we expect from the disagreement for ${}^{1}L^{(\perp)}(\theta)$ evident in Fig. 16(b). A comparison with Fig. 16(b) shows that the disagreement in the singlet angular momentum transfer around the peak at 30° arises from a discrepancy in the $M_L=-1$ channel.

3. *Exchange asymmetries*

Another perspective on the information contained in the spin-channel amplitudes is afforded by the $3s\to 3p$ exchange asymmetries $A^{(ex)}_{M_L}(\theta)$. These quantities have been reported by McClelland, Kelley, and Celotta [9] and we compare their results, determined via time reversal from data taken in superelastic $3p\to 3s$ experiments, to various theoretical results in Fig. 18. In particular, we have plotted this quantity versus energy at a scattering

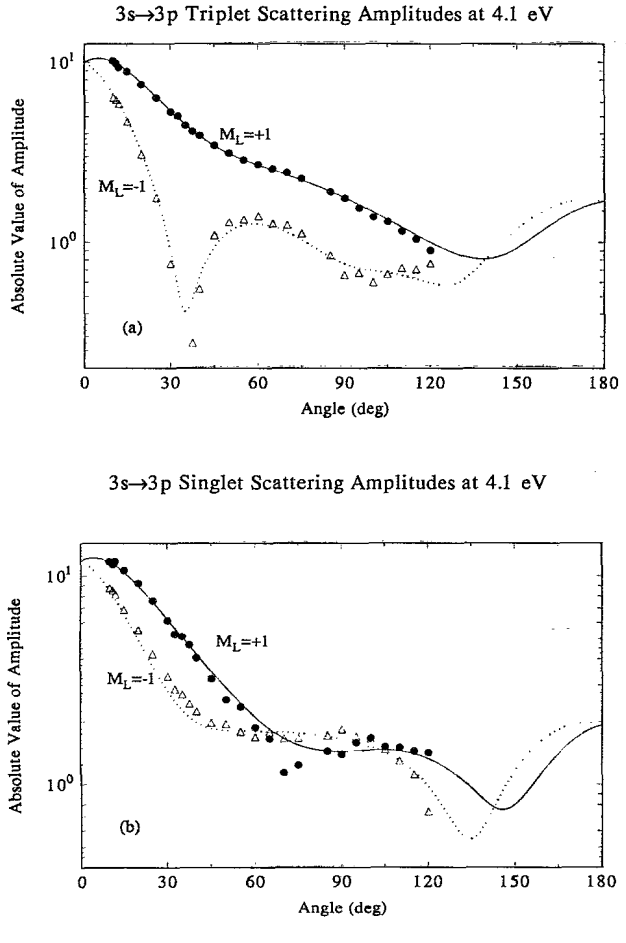

FIG. 17. Magnitudes of the $3s\to 3p$ (a) triplet and (b) singlet scattering amplitudes $|{}^{2S+1}f_{\pm 1,0}(\theta)|$. For comparison purposes we have constructed "experimental" amplitudes by combining $r_{3s\to 3p}(\theta)$, ${}^{1}L^{(\perp)}_{3s\to 3p}(\theta)$, and ${}^{3}L^{(\perp)}_{3s\to 3p}(\theta)$ from measurements at 4.1 eV by McClelland, Kelley, and Celotta [11] with our theoretical differential cross sections to obtain the magnitudes of the scattering amplitudes for $M_L=+1$ (solid circles) and for $M_L=-1$ (open triangles). The purely theoretical results (from 10CC calculations) are also given for $M_L=-1$ (solid curve) and $M_L=-1$ (dots).

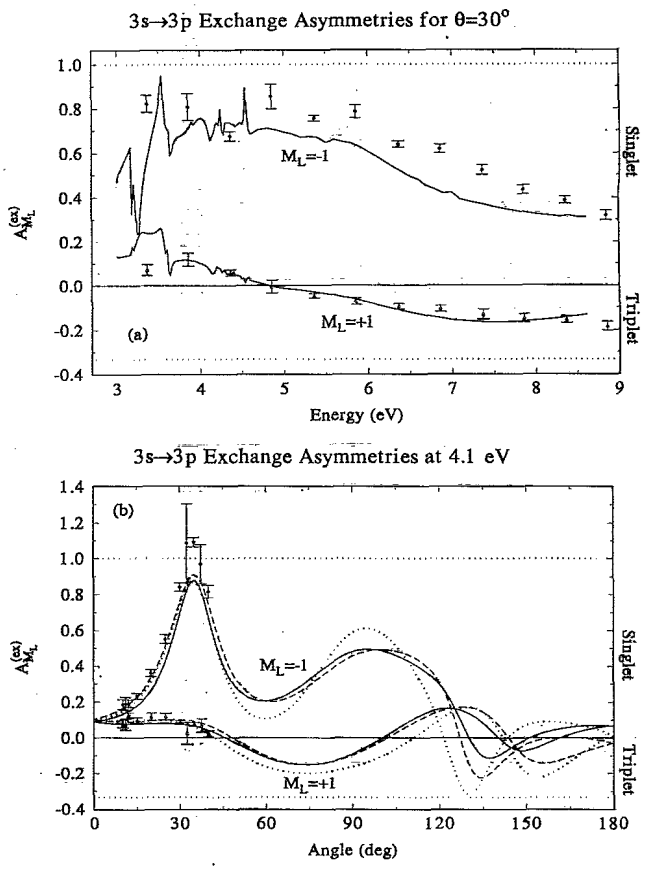

FIG. 18. (a) Comparison of 10CC theoretical exchange asymmetries for $M_L=\pm 1$ for fixed angle as a function of energy to experimental data taken at 30°. Theoretical data are shown for scattering angles of 30° (solid curve). (b) Theoretical (10CC) exchange asymmetries for $M_L=\pm 1$ at 4.0 eV (dashed line), 4.1 eV (solid line), and 4.2 eV (dotted line). In (a) and (b) the experimental data are those of McClelland, Kelley, and Celotta [9]. The dotted horizontal lines indicate maximum and minimum allowed values of this quantity.

angle of 30° in Fig. 18(a) and versus scattering angle in Fig. 18(b). The most striking feature in these figures is the difference between the asymmetries for $M_L = +1$ and -1. In the former case, scattering is almost equally probable into the singlet and the triplet spin channels, while for the latter, the flux into these spin channels varies with angle.

The measured $3s \rightarrow 3p$ asymmetries of McClelland, Kelley, and Celotta [9] for $M_L = +1$ agree very well with our 10CC results, while for $M_L = -1$ we find comparable agreement except near 30°, where the experiment finds the peak to be significantly larger than does the theory. Note that the curves for nearby energies in Fig. 18(b) indicate that this difference is not due to an energy mismatch. Finally, we note that the energy dependence in Fig. 18(a) reflects the complex variation with energy of the $3s \rightarrow 3p$ ICS reported in Ref. [1].

4. *Relative phase angles and the polarization ratio*

In addition to the four parameters that determine the magnitude of the $s \rightarrow p$ scattering amplitudes, three relative phase angles are required for a complete description of the collision. As discussed in Sec. II D and Eq. (42), we have chosen the singlet-triplet phase angle $\Delta_{+1,0}(\theta)$ and the two alignment angles ${}^{2\mathcal{S}+1}\gamma(\theta)$. The convergence behavior of these quantities at 4.1 eV is shown in Figs. 19 and 20, respectively. Here we see that the triplet-singlet phase angle $\Delta_{+1,0}(\theta)$ requires a more complete description of the target than the 7CC basis provides; we note also the excellent agreement between Bray's values and our converged 10CC results.

While the triplet alignment angle is well represented in the 7CC calculation, the singlet angle is problematic, though less so than the singlet angular-momentum transfer. The differences between the 4CC, 7CC, and 10CC results are significant and at large angles our results disagree with values calculated by Bray even though the 11CC results show our 10CC values to be well converged.

Unfortunately, there are no direct measurements of the relative phase angles; Hermann [7], however, measured a spin-averaged alignment angle γ at 5.1 eV in experiments with unpolarized electrons. In addition, the measurement by Hegemann *et al.* [17] of the inelastic polarization ratio depends on the two triplet-singlet phase angles $\Delta_{M_L,0}$, as well as the triplet-to-singlet ratio and the angular-momentum transfer. With $r(\theta)$ and ${}^{2\mathcal{S}+1}L^{(1)}_{3s\rightarrow 3p}(\theta)$ in hand, one can therefore determine information about the triplet-singlet phase angle, and Andersen and Bartschat [52] have proposed an ingenious theoretical scheme to extract these angles from measured

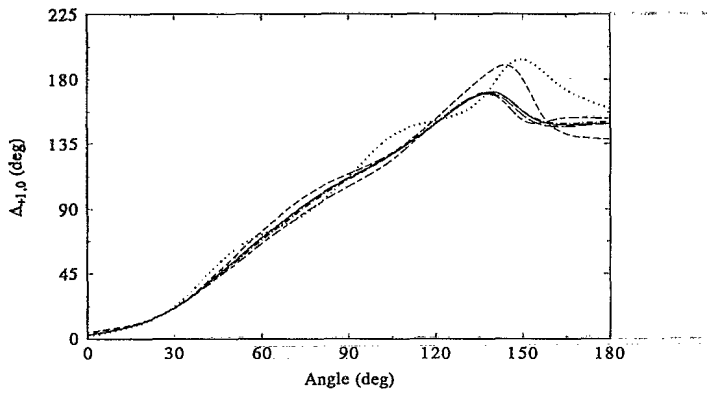

FIG. 19. Convergence of the $3s \rightarrow 3p$ triplet-singlet phase angle $\Delta_{+1,0}(\theta)$ at 4.1 eV as demonstrated by values calculated from R matrices based on the following models: 11CC(6s) (long-dashed curve), 11CC(6p) (short-dashed curve), 10CC(ND) (dot-dashed curve), 10CC (solid curve), 7CC (medium dashed curve), and 4CC (dotted curve). Also shown are theoretical data calculated by Bray and McCarthy [39] (long-dash–short-dashed curve).

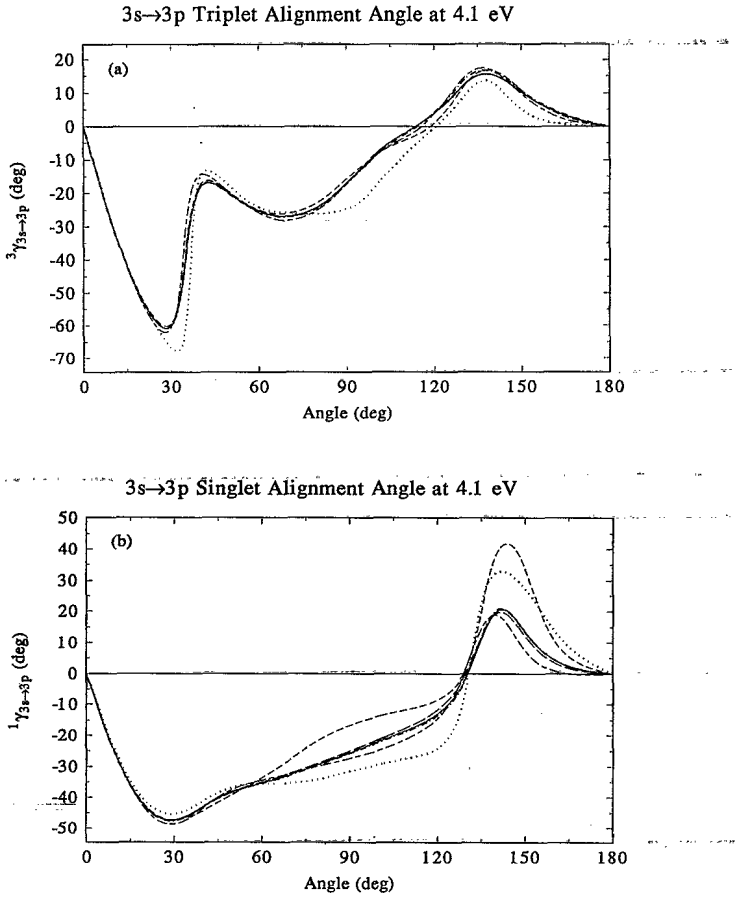

FIG. 20. Convergence behavior of the $3s \rightarrow 3p$ (a) triplet and (b) singlet alignment angles ${}^{2\mathcal{S}+1}\gamma(\theta)$ at 4.1 eV from calculations based on the following models: 11CC(6s) (long-dashed curve), 11CC(6p) (short-dashed curve), 10CC(ND) (dot-dashed curve), 10CC (solid curve), 7CC (medium dashed curve), and 4CC (dotted curve). Also shown are theoretical data calculated by Bray and McCarthy [39] (long-dash–short-dashed curve).

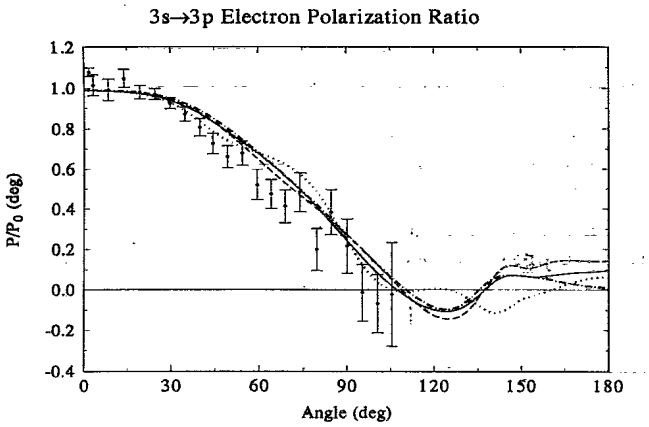

FIG. 21. Electron polarization ratio P/P_0 for inelastic $3s \rightarrow 3p$ scattering at 4.0 eV. Experimental data points were measured by Hegemann *et al.* [17]. Our theoretical data are shown for the following models and energies: 10CC at 4.1 eV (solid curve), 10CC at 4.0 eV (long-dash–short-dashed curve), 7CC at 4.0 eV (medium-dashed curve), and 4CC at 4.0 eV (dotted curve).

data.

The inelastic polarization ratio in Fig. 21 exhibits dramatic exchange effects for all scattering angles except the forward direction. By contrast to its angle dependence, this ratio is insensitive to small changes in energy. This supports the validity of using these data and those of McClelland, Kelley, and Celotta [11], in spite of the energy mismatch between the measurements, in the procedure recommended by Andersen and Bartschat [52].

VI. CONCLUSION

The level of concordance seen in Sec. V between theoretical and measured OA parameters for the $3s \rightarrow 3s$ and $3s \rightarrow 3p$ transitions at experimental energies from 1.0 to 4.1 eV supports the wider-ranging survey of trends and features in these parameters (and in others not yet measured) from threshold to 8.6 eV in the three-dimensional figures of Sec. IV. At energies near the ionization threshold at 5.14 eV, however, the true values of some of these parameters may exhibit small-scale but pronounced structures (akin to those near 4 eV) that do not appear in the present theoretical results, because even our most extensive close-coupling calculations include no target states above 4.6 eV, the threshold of the $6p$ excited state of the Na valence electron. This omission should not, however, affect significantly the overall trends apparent in these figures. We hope that the availability of these overviews of the data will help guide future measurements (e.g., away from energies where these parameters are especially small).

Apart from these small-scale high-energy considerations and our neglect of bound and continuum spin-orbit interactions—an approximation that should be excellent for the e-Na system—the primary aspect of the present theoretical formulation that might affect the accuracy of these results is the neglect of virtual excitation of the valence electron to the continuum. Comparisons to the theoretical results of Bray indicate that, at least at 4.1 eV, this approximation also is very good.

The state-space formulation in Sec. II of the theory of orientation and alignment in electron-atom scattering for experiments involving initial-state preparation and/or final-state analysis can easily be extended to other transitions and systems. If, for example, characterization of the target states requires a coupling scheme other than the LS representation of Eq. (8), one need only replace $\mathcal{C}_{nL}^{(A)}$ with the appropriate eigenspace as defined by the scattering event of interest. Of course, additional modifications would be required if the spin-orbit interaction were significantly stronger than in the e-Na system.

In the final paper in this series, we shall complete thus study of low-energy e-Na scattering by extending the present formulation and the calculations here and in Ref. [1] of DCSs, ICSs, and OA parameters to excitation from excited initial states of Na.

ACKNOWLEDGMENTS

We would like to thank Dr. Eric Layton, Dr. Nils Andersen, and Dr. Chris Greene for invaluable conversations concerning various aspects of this research and to acknowledge Dr. Werner Eissner and Dr. Kenneth Bell for providing improved unpublished versions of the R-matrix and asymptotic codes. We are grateful to Dr. Terry L. Goforth for her help with the experimental data and to Dr. R. E. Scholten, Dr. M. H. Kelley, and Dr. I. Bray for sending us their data. M.A.M. and B.L.W. would also like to thank the Joint Institute for Laboratory Astrophysics for hospitality during the writing of this manuscript. This work used the Cray facilities at NIST (Gaithersburg, MD), NERSC (Livermore, CA), and NCSA (San Diego, CA). M.A.M. gratefully acknowledges the support of the National Science Foundation under Grant No. PHY-9408977, as does K.B.M. under Grant No. PHY-9122377 and K.B. under Grant No. PHY-9318377. The work of W.K.T. and D.W.N. was supported in part by NSF Grant No. PHY-9012244 to the University of Colorado. Finally, B.L.W. thanks the Colorado College for partial research support.

[1] W. K. Trail, M. A. Morrison, Hsiao-Ling Zhou, B. L. Whitten, K. Bartschat, K. B. MacAdam, T. L. Goforth, and D. W. Norcross, Phys. Rev. A **49**, 3620 (1994).

[2] H. W. Hermann and I. V. Hertel, Comments At. Mol. Phys. **12**, 61 (1982).

[3] H. W. Hermann and I. V. Hertel, Comments At. Mol. Phys. **12**, 127 (1982).

[4] H. W. Hermann, I. V. Hertel, and M. H. Kelley, J. Phys. B **13**, 3465 (1980).

[5] H. W. Hermann and I. V. Hertel, Z. Phys. A **307**, 89

(1982).
[6] I. V. Hertel, M. H. Kelley, and J. J. McClelland, Z. Phys. D **6**, 163 (1987).
[7] H. W. Hermann, Ph.D. thesis, Universität Kaiserslautern, 1979 (unpublished).
[8] J. J. McClelland, M. H. Kelley, and R. J. Celotta, Phys. Rev. Lett. **55**, 688 (1985).
[9] J. J. McClelland, M. H. Kelley, and R. J. Celotta, Phys. Rev. Lett. **56**, 1362 (1986).
[10] R. E. Scholten, S. R. Lorentz, J. J. McClelland, M. H. Kelley, and R. Celotta, J. Phys. B **24**, L653 (1991).
[11] J. J. McClelland, M. H. Kelley, and R. J. Celotta, Phys. Rev. A **40**, 2321 (1989).
[12] M. H. Kelley, J. J. McClelland, S. R. Lorentz, R. E. Scholten, and R. J. Celotta, in *Correlations and Polarization in Electronic and Atomic Collisions and* $(e,2e)$ *Reactions,* edited by P. J. O. Teubner and E. Weigold, IOP Conf. Proc. No. 122 (Institute of Physics, London, 1992), p. 23.
[13] J. J. McClelland, S. R. Lorentz, R. E. Scholten, M. H. Kelley, and R. J. Celotta, Phys. Rev. A **46**, 6079 (1992).
[14] R. E. Scholten, J. J. McClelland, M. H. Kelley, and R. J. Celotta, Phys. Rev. A **47**, 3000 (1993).
[15] S. R. Lorentz, R. E. Scholten, J. J. McClelland, M. H. Kelley, and R. J. Celotta, Phys. Rev. Lett. **67**, 3761 (1991).
[16] V. Nickich, T. Hegemann, M. Bartsch, and G. F. Hanne, Z. Phys. D **16**, 261 (1990).
[17] T. Hegemann, M. Oberste-Vorth, R. Vogsts, and G. F. Hanne, Phys. Rev. Lett. **66**, 2968 (1991).
[18] *Coherence and Correlation in Atomic Collisions,* edited by H. Kleinpoppen and J. F. Williams (Plenum, New York, 1980).
[19] K. Blum and H. Kleinpoppen, Adv. At. Mol. Phys. **19**, 187 (1983).
[20] J. Slevin, Rep. Prog. Phys. **47**, 461 (1984).
[21] G. F. Hanne, Phys. Rep. **95**, 95 (1983).
[22] G. Hanne, in *Proceedings of the Seventeenth International Conference on the Physics of Electronic and Atomic Collisions,* edited by W. R. MacGillivray, I. E. McCarthy, and M. C. Standage (Hilger, New York, 1992), p. 199.
[23] G. F. Hanne, in *Coherence in Atomic Collision Physics,* edited by H. J. Beyer, K. Blum, and R. Hippler (Plenum, New York, 1988).
[24] J. Kessler, *Polarized Electrons,* 2nd ed. (Springer-Verlag, Berlin, 1985).
[25] J. Kessler, Adv. At. Mol. Phys. **27**, 81 (1991).
[26] W. R. MacGillivray and M. C. Standage, in *Coherence in Atomic Collision Physics* (Ref. [23]), p. 103.
[27] N. Andersen, J. Gallagher, and I. V. Hertel, Phys. Rep. **165**, 1 (1988).
[28] I. C. Percival and M. J. Seaton, Philos. Trans. R. Soc. London Ser. A **251**, 113 (1958).
[29] B. Bederson, Comments At. Mol. Phys. **2**, 160 (1971).
[30] K. Rubin, B. Bederson, M. Goldstein, and R. E. Collins, Phys. Rev. **182**, 201 (1969).
[31] G. Csanak, S. Trajmar, J. C. Nickel, G. F. Hanne, J. W. McConkey, T. L. Gay, and M. A. Khakoo, Comments At. Mol. Phys. **30**, 165 (1994).
[32] K. Bartschat, Phys. Rep. **180**, 1 (1989).
[33] B. Bederson, Comments At. Mol. Phys. **1**, 41 (1969).
[34] B. Bederson, Comments At. Mol. Phys. **1**, 65 (1969).
[35] B. Bederson, Comments At. Mol. Phys. **2**, 1601 (1970).
[36] K. Rubin, B. Bederson, M. Goldstein, and R. E. Collins, Phys. Rev. A **182**, 201 (1969).
[37] H. Kleinpoppen, Phys. Rev. A **3**, 2015 (1971).
[38] I. Bray and I. E. McCarthy, Phys. Rev. A **46**, 6995 (1992).
[39] I. Bray and I. E. McCarthy, Phys. Rev. A **47**, 317 (1993).
[40] I. Bray, Phys. Rev. A **49**, 1066 (1994).
[41] I. Bray, Phys. Rev. A **49**, R1 (1994).
[42] I. Bray and A. T. Stebovics, Comput. Phys. Commun. **85**, 1 (1995).
[43] D. L. Moores and D. W. Norcross, J. Phys. B **5**, 1482 (1972).
[44] D. A. Varshalovich, A. N. Moskalev, and V. K. Khersonskii, *Quantum Theory of Angular Momentum* (World Scientific, Singapore, 1988).
[45] R. N. Zare, *Angular Momentum: Understanding Spatial Aspects in Chemistry and Physics* (Wiley, New York, 1988).
[46] K. Blum, *Density Matrix Theory and Applications* (Plenum, New York, 1981).
[47] D. ter Haar, Rep. Prog. Phys. **24**, 304 (1961).
[48] W. R. MacGillivray and M. C. Standage, Phys. Rep. **168**, 1 (1988).
[49] J. R. Taylor, *Scattering Theory* (Wiley, New York, 1972).
[50] W. R. MacGillivray and M. C. Standage, Comments At. Mol. Phys. **26**, 179 (1991).
[51] N. Andersen and K. Bartschat, Comments At. Mol. Phys. **29**, 157 (1993).
[52] N. Andersen and K. Bartschat, Phys. Rev. A **49**, 4243 (1994).
[53] W. Gehenn and E. Reichert, Z. Phys. **254**, 28 (1972).
[54] A special problem arising from the definition of the elastic triplet-singlet phase angle occurs at angles near 140°. At 4.1 eV, the magnitudes of the real and the imaginary parts of the singlet $3s \rightarrow 3s$ scattering amplitudes in this angular range are nearly zero. This makes calculating their relative phase problematic and, if possible at all, acutely sensitive to fine points of the calculation. At 4.1 eV, the real and the imaginary parts of the 4CC amplitudes near 140° happen to be coincident and both nearly zero; this accident causes rapid unphysical changes in $\Delta_{0,0}(\theta)$ near this angle, which is why we do not show 4CC results here. This accidental coincidence does not occur in results from the 7CC and the 10CC calculations. To explore this point more thoroughly we show results from a 7CC calculation, which completes the $n=4$ manifold by including in addition to the states of the 4CC study those for $4p$, $4d$, and $4f$, sufficient to converge $\Delta_{0,0}(\theta)$ at all angles.
[55] X. L. Han, G. W. Schinn, and A. Gallagher, Phys. Rev. A **38**, 535 (1988).
[56] X. L. Han, G. W. Schinn, and A. Gallagher, Phys. Rev. A **42**, 1245 (1990).